A novel thermomechanical modelling framework

in metal additive manufacturing process modelling

Q.Zhu 4820975

Thesis Report

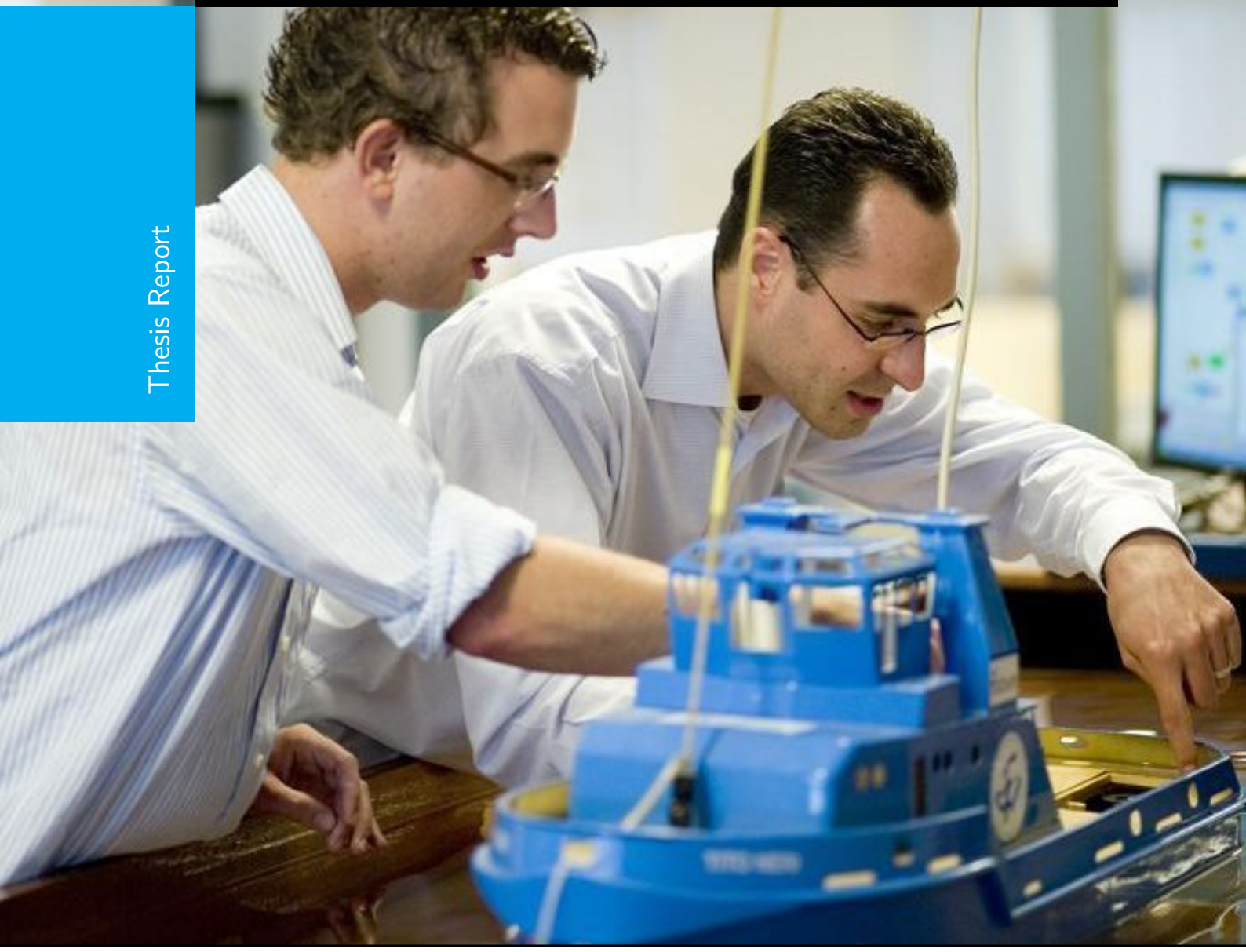

TU Delft Delft University of Technology

Structural Optimization and Mechanics

A novel thermomechanical modelling framework

in metal additive manufacturing process modelling

Thesis Reoprt

Q.Zhu 4820975

December 6, 2020

Faculty of Mechanical, Maritime and Materials Engineering (3mE) · Delft University of Technology

Abstract

Powder bed fusion (PBF) is a widely used metal additive manufacturing method where a part is built with almost no limitation on its geometrical layout. However, parts built by PBF typically suffer from distortions and residual stresses which depend on the PBF processing conditions and the geometrical layout of the part. In order to investigate this relation, a new computational tool is presented. The unique property of our methodology is to keep the total number of degrees of freedom constant by utilising a moving grid to represent a growing part with time. Thermal transients are calculated and are coupled to a mechanical boundary value problem to evaluate the evolution of temperature history and residual stresses. The significant gain in the computational efficiency of the moving grid technique is demonstrated in comparison to the state of the art models available in the literature.

Table of Contents

List of Figures

List of Tables

Acknowledgements

I would like to thank my supervisor Dr. Can Ayas for his selfless support on my thesis, he gave me a lot of significant guidance when I was trapped in a dilemma. I also learn from him not only for his rigorous attitude towards scientific research, but also for his kindness to colleagues and students. It's my great honor to be one of his master students and do the thesis with him.

Also I would like to thank my friends, Ziyulong Wang, Haoyu Zhu, Jiajin Li, Yuheng Yan, all my classmates in PME department, the Chinese friends I met in Delft, roommates in unit 17 and unit 121, teammates in DCF and whoever helped during my stay in Netherlands, we went through the toughest time together in this special year.

Next I would like to express my gratitude to my parents who gave me finical support for my study and also encouraged me when I was upset.

At last I want to thank my dearest Haiyin, we finally met after 8 months separation. A brave girl comes to a foreign country ten thousand kilometers away from home only to meet her boyfriend and this is our love story.

It's a long run to finish my thesis and it's an unforgettable experience to be aside with a group of talented people. I will always remember the 2 years and a half time in my life living and studying in Delft, these shining days will be my best memory.

Delft, University of Technology Qingyuan Zhu
December 6, 2020

Chapter 1

Introduction

Evolved from the concept of rapid prototyping in the 1980's, additive manufacturing technology (AM) has been considered as the most revolutionary manufacturing approach in modern industry since it breaks through the shape limitation when using conventional subtractive manufacturing methodologies. These advances highly promote the development of AM over the past two decades [7, 1]. By the end of the 2013, the market demand has grown to 3 billion dollars and in 2017, this number grew to 6 billion dollars, evidencing a maturing industry. [8, 9].

Currently, up to 7 different AM processes have been defined by ASTM and they are widely used in building industry (3D printing house), aerospace engineering (fuselage design and powertrain design) and medical field(organ implant). As one of the seven processes, powder bed fusion (PBF) is capable of dealing with various type of materials including metal powder, which makes it the predominant metal AM technology. Fig. 1-1 illustrates the working principle of PBF. A powder bed is generated by a roller raking powder from delivery system. Afterwards, a heat source scans over the cross section according to the product shape. The powder is melted and fused and subsequently forms a solid layer. Next, the build platform is lowered and a new layer of metal powder will be delivered by the roller. This process is repeated until a 3 dimensional model is built by depositing layer upon layer.

Due to the different types of heat source, PBF can be further subdivided into selective laser melting(SLM) and selective electron beam melting(SEBM). These 2 processes are more or less the same only with slightly difference in the following aspects:

- The penetration depth of laser beam is just few nanometers but the electrons penetrate into a micrometer scale depth.
- SEBM operates in a vacuum chamber while SLM usually works in a inert shielding gas atmosphere.
- SEBM operates with a preheating while SLM usually not.
- SEBM can only operate with conductors while SLM has more options for material.

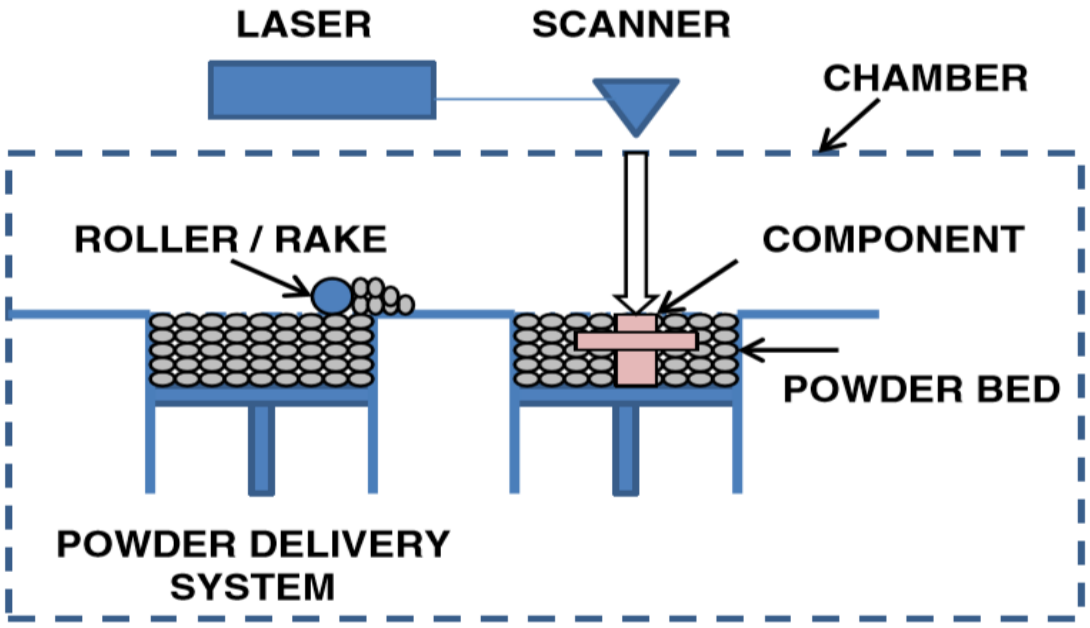

Figure 1-1: Working principle of PBF process reproduced from [1]. A powder bed is generated by a roller raking powder from delivery system. Afterwards, a heat source scans over the cross section according to the product shape. The powder will be melted and fused and subsequently forms a solid layer. Next, the piston of the powder bed will be lowered and a new layer of metal powder will be delivered by the roller. This process is repeated until a 3 dimensional model is built by depositing layer upon layer.

These differences will change the way to model the heat source and the heat boundary conditions. In this study, we mainly pay attention to SLM process, the details with respect to model SEBM process is out of the scope of our work [7, 1, 10].

Although with a promising future, SLM still faces several challenges that need to be solved. One main challenge is the uncertainty in product quality induced by both the material properties and the process parameters. The temperature dependent material properties, designing strategy such as scanning pattern, inclination in work piece will all lead to the differences in temperature distribution during the AM process. Also, complex thermal and mechanical phenomenon during the manufacturing process leads to defects such as distortion and crack due to residual stress, which are detrimental for the strength. These defects can be attributed to the variation in process parameters and the trial-and-error principle is used to determine the underlying correlations between process parameters and product quality. However, the typical experimental approach usually costs a lot of time and money. Consequently, an efficient and accurate numerical model is needed to get the insight about the physics of SLM process by simulation whose results can further give us the guidelines on optimizaiton process and assist us to improve the in-process monitoring on crucial regions where the crack and distortion might occur.

SLM is an inherently multiscale phenomenon. For instance, in length scale mean particle size is micrometers while the whole component can be centimeters. As for time scale, the time for solid-liquid phase transformation only take a few milliseconds but it will take several

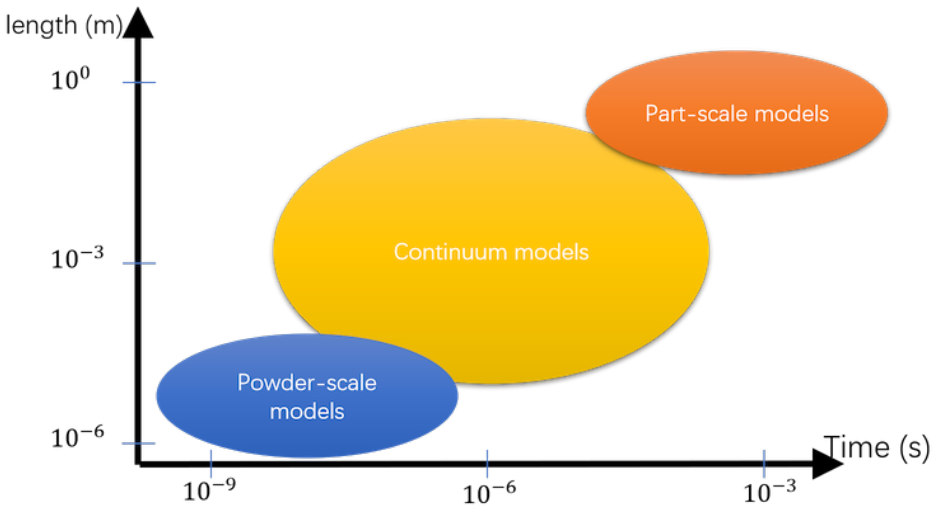

Figure 1-2: Multi-scale modelling for SLM process. Different modelling approaches use different time scales and length scales. Powder-scale model usually builds on length scale at microcmeter and time scale at nanosecond while part-scale builds on length scale at millimeter and time scale at millisecond. The continuum model falls in the middle.

hours even a day to finish a component [4]. Different modelling approaches, which is shown in Fig. 1-2, use different level of assumptions and approximations. For instance, the part-scale models gloss over the laser spot size, while the powder scale models usually cannot simulate a reasonable part dimension. That is to say, these variations in assumptions and approximations will definitely have an impact on what we can observe from the simulation results.

In the next 2 chapters of the report we will focus on the specific methods on SLM process modeling. Chapter 2 will explain the modelling approach on powder scale model and continuum model with simulation results of representative examples. Chapter 3 will introduce a new part-scale model based on a moving mesh approach which will dramatically improve computational efficiency [11, 8].

Chapter 2

Modelling approaches for SLM

The complex nature of local melting makes the whole SLM process not fully controllable and predictable so far and some of the physical phenomena can not be captured by a coarse spatial and time resolution in simulation. For example, it's impossible to determine the temperature transients due to a localised laser beam by a coarse spatial discretization since the diameter of a laser beam in SLM is usually measured in micrometers [12, 2, 13]. This also holds in time scale, the solid-liquid-solid phase transformation only takes few milliseconds, if the time step is larger than that interval then the transformation will not be reflected in the numerical modelling. Fig. 2-1 exhibits the physical phenomena occur in the laser melting process. Among these phenomena, heat conduction, convection, radiation and absorption basically describe the heat transfer modes in SLM process, melting/solidification, shrinkage mainly focus on issues in solid/liquid phase change on top layers. Another important aspect is melt pool, which is the small area of melted metal powder. To build a melt pool model usually fluid dynamics issues such as marangoni-convection, capillary forces as well as gravity are taken into account. Not all the studies consider melt pool dynamics part in a single numerical model because it's always computational expensive in mathematical modelling, but a basic SLM model requires at least model for heat source, heat conduction in solid phase and convection between air in work chamber and layer.

2-1 Powder-scale model

As the name suggests, the length scale of the powder-scale model is usually taken as one tenth of the powder diameter [8]. Although there's a variation in powder size, a spatial mesh in micrometer level for a single particle is often reasonable for powder-scale model. In the model, the powder particles are regarded as ideal spheres which are represented by micrometer level spatial mesh as mentioned above. In order to simulate the random distribution of the powder bed, the rain drop method has been utilized for random packing in which the falling particles can rotate freely until a final steady state is reached (e.g. local potential minimum). However, the powder bed generated by the rain drop method is usually denser than reality. Therefore, to achieve a reasonable density some of the particles are randomly removed. Alternatively,

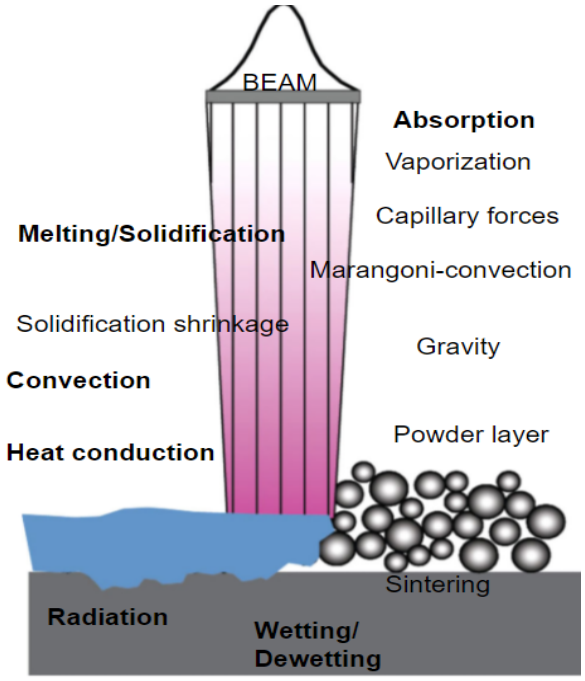

Figure 2-1: All possible physical phenomenon during selective laser melting. Vaporization, capillary forces, marangoni-convection, gravity, wetting/sintering are mainly about hydrodynamics, while the rests are about thermodynamic. The bold face words are the parts that commonly seen in a SLM thermal model. [2].

free-fall discrete element method which accounts for the rolling and raking process of the powder deliver system is employed [8, 2, 14].

During the SLM process, a laser beam will scan over the powder bed and the laser heat source will be modelled as a bell-shaped Gaussian energy density function. This surface heat source will move along the scanning track locally melting particles. The scanning and melting process can be achieved by checking the nodal temperature information so that a interface can be defined between solid elements and liquid elements. Next, physical properties of elements which are determined in melting state will be updated as liquid and subsequently, back to solid after solidification. In addition, the laser-material interaction needs to be considered during the scanning and melting process. When laser interacts with powder particles, the photons of the laser will go through several reflections and thereby penetrate much deeper than it would have in a bulk material. A ray-tracing Monte Carlo method can be applied to model this beam absorption process. Sometimes for the sake of simplicity, the reflection process is neglected and a fixed absorption coefficient is assigned [8, 2, 3].

The heat transfer in SLM process contains thermal conduction, radiation and convection. For a simple cube sample, the bottom surface connected with the ground is usually can be seen as under constant temperature or insulated and the interface between powder domain and solid domain can be modelled as insulated or a comparatively weak thermal conduction, which is due to the porosity in powder bed weakens the heat conduction ability in powder domain. Within the solid domain, the heat conduction is the dominant feature. Most complicated part comes at the top surface, the heat dissipation includes convection and radiation which form a combined boundary condition [15]. In many studies, the heat exchange via radiation

and convection is omitted to reduce the computational effort and the irradiation of laser beam is the only energy source from the top [14]. Additionally, the boundary conditions between lateral side and external environment can be seen as a mixed boundary including heat convection and radiation. A simpler option is to again use a insulted boundary by assuming the process is going on in a closed chamber [11, 16, 17]. The governing equation is given in the form of thermal energy conservation. Due to the influence of phase transformation, this governing equation is better to be given in the form of enthalpy rather than temperature [2, 5]. Furthermore, considering the fact that the area under the direct irradiation of laser beam will no longer be solid, the Navier-Stokes equation will be introduced to describe the hydrodynamics in the melt pool [2].

The dynamics of melt pool, which is determined mainly by process parameters, will greatly affect the quality of the final component in terms of porosity, surface roughness. Therefore, the hydrodynamic effects that change the melt pool dynamics such as surface tension and evaporation need to be analyzed in the numerical model, which is known as the Lattice-Boltzmann method. This method is an computational approach for fluid dynamics. Instead of solving the Navier–Stokes equations directly, a fluid density on a lattice is simulated with streaming and collision (relaxation) processes.

As one of the most significant aspect of powder-scale model, many of the provided studies focus on how the component quality will change by altering the process parameters. For instance, Körner *et al.*(2010) [2] studied the line morphology under different beam power and scanning speed, which can be seen in Fig. 2-2. Fig. 2-2 (a) shows line morphology with increasing line energy (by decreasing scan speed at constant beam power). It's observed that the metal powder are not or just slightly molten under a low line energy. By increasing the line energy, the metal powder will melt into small droplets and as the line energy continues to increase, these small droplets will gradually stick together to be a closed molten and re-solidified region. Fig. 2-2 (b) shows the line melting and solidification with constant line energy but for different scan speed and beam power, it's found that the melting pattern of metal powder seems not dependent on processing parameters under a constant line speed. Francois et al.(2017) [3] used a self-designed multiphysics code called ALE3D researching the melt pool geometry on a single track considering the surface tension and vaporization recoil, the simulation results are shown in Fig. 2-3, and based on these results we can subdivide the melt pool into three different regions: the depression region at the laser spot, the tail end region of the melt track located near the end and the transition region in between. Such kind of subdivision is made because of the exponential dominance of the recoil force at the depression and the dominance of Marangoni surface tension effects in the cooler transition and tail regions Lavery *et al.* (2014) [4] developed a 3D Lattice-Boltzmann code in FORTRAN to simulate the laser melting process for 316L steel powder, which is shown in Fig. 2-4. The temperature change of powder bed can be clearly seen in Fig. 2-4 when a laser scans over it. There are more powder-scale researches focus on other aspects can be found in review literatures [8, 14]. In addition, some scientists also work on a micro-scale research which mainly pay attention to the grain growth and grain boundary formation during SLM process. These investigations may give us ideas on stress distribution and distortions [8, 3, 13].

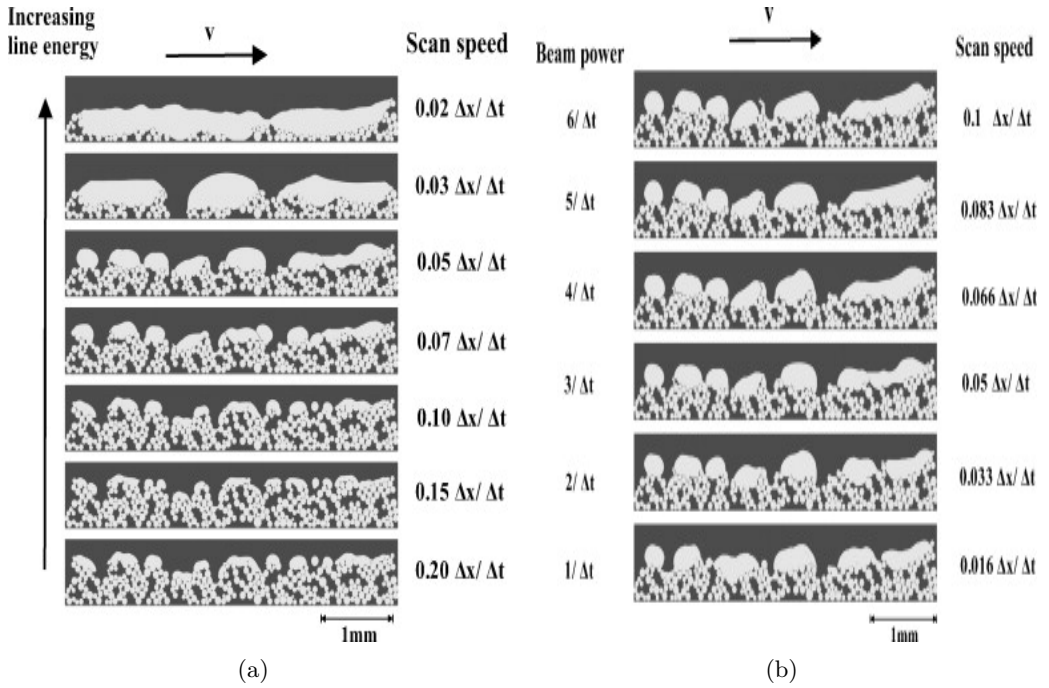

Figure 2-2: Line morphology under different line energy, beam power and scan speed. (a) shows line morphology as a function of the line energy and (b) shows line morphology at constant line energy for different scan speeds and beam powers, reproduced from [2]. Time scale and length scale used here are $\Delta x = 5.0 \times 10^{-6}$m and $\Delta t = 2.2 \times 10^{-7}$s respectively, the duration of the beam irradiation is 1440 time steps (Δt).

2-2 Continuum models

A powder-scale model simulation is always computationally expensive since a fine discretization in both time and length scale is required for powder-scale model, and fluid dynamics analysis for melt pool will occupy a lot of computing resources. A simple calculation can be used to prove how large the demand for element numbers is when building a powder-scale model. In a SEBM powder-scale modelling, the mean particle diameter can be around 50 μm so the element size in thermal analysis can be taken as 5 μm. If that is the case, a small domain with the volume at 1 mm^3 requires 8 billion cubic elements. The number of elements could be more for SLM since the mean particle size will be down to approximately 10 μm.

With the purpose to reduce the burden on computation, on the one hand, the requirement on time and spatial resolution could be lower since there's no need to resolve the particle. On the other hand, the computation demanding hydrodynamics part including wetting effect, capillary and surface tension, which depend on surface curvature defined by modelling the particles as perfect spheres, can be neglected. It's still possible to capture a melt pool by continuum model but its geometry is just simply predicted by the temperature field [8].

Additionally, the boundary between metal particles and porous part vanishes since metal powders are no longer resolvable in a continuum model. In order to assign the material property, approaches like interpolation between zero and value of bulk material according to relative porosity is often applied while in some studies the data from empirical model is

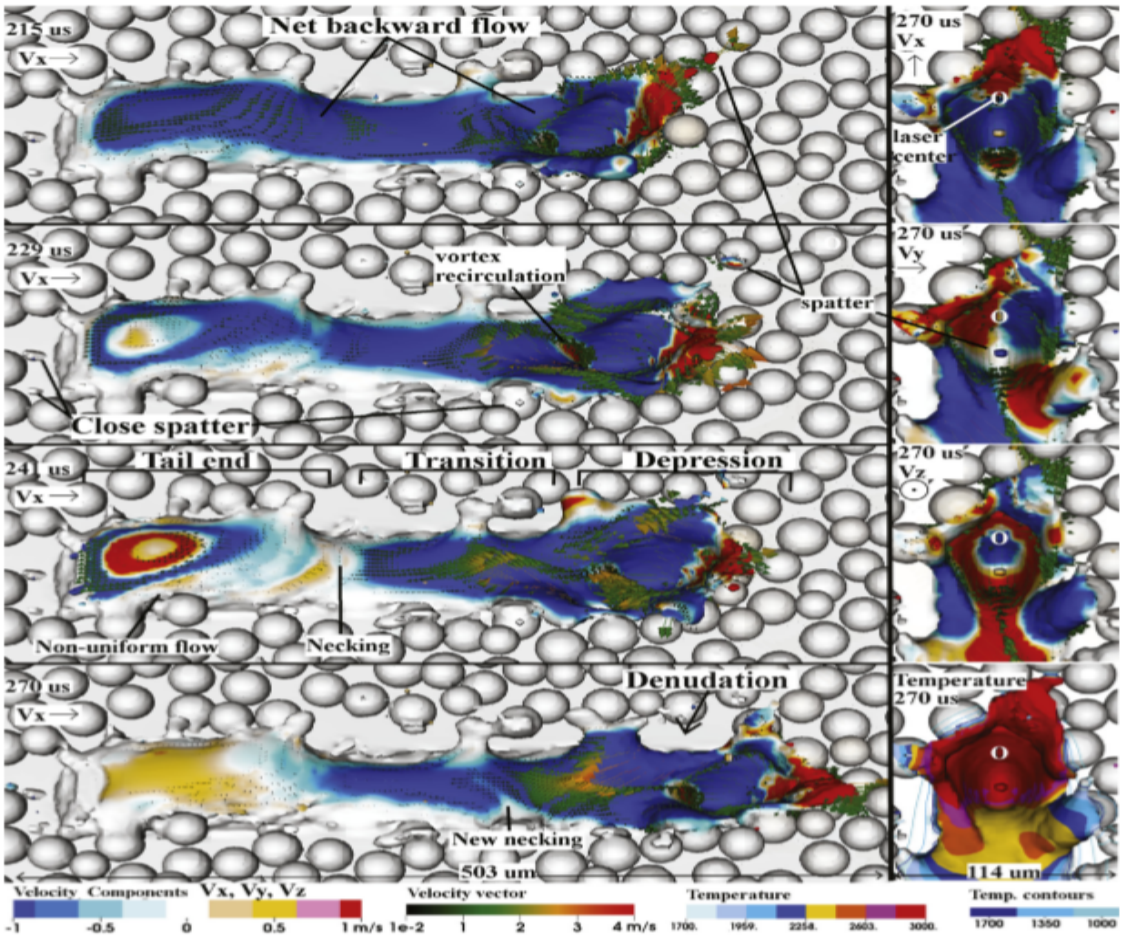

Figure 2-3: AEL3D simulation reproduced from [3] and these time snapshots show spattering and denudation of the melt flow. Compared to forward flow (red color, $V_x < 0$), the melt has a large backward flow (blue color, $V_x < 0$). This backward flow will break up later in time at the necking. Panel on the right shows a magnified view at 270 μs (flow retated by $+90°$), in which the velocity components (V_x, V_y, V_z) and and the temperature distribution at the depression can be observed. Capital O shows the laser center is not at the bottom of the depression.

employed [8, 5, 12, 10, 6]. As a matter of fact, almost all the thermal and mechanical properties will change as the temperature grows. Luo and Zhao (2018) [11] give some useful empirical models on how density, thermal conductivity and specific heat will change as a function of temperature. Childs et al.(1999) [18] studied mechanical properties of an amorphous polymer in selective laser sintering, during which they take into account nonlinear thermal properties. But nonlinear thermal properties also bring nonlinearity in the governing equation, thus many studies prefer to use mean constant value in the simulation.

Surface and volume heat sources are still usable in continuum model, furthermore, in some cases, a line heat source is applied to reduce the computational effort [11]. Generation of the growing part in continuum model is simulated by using element activation method. During the simulation, all the necessary elements are divided into 'active' and 'inactive' domain, those elements above the base plate are deactivated in the beginning and become active layer by

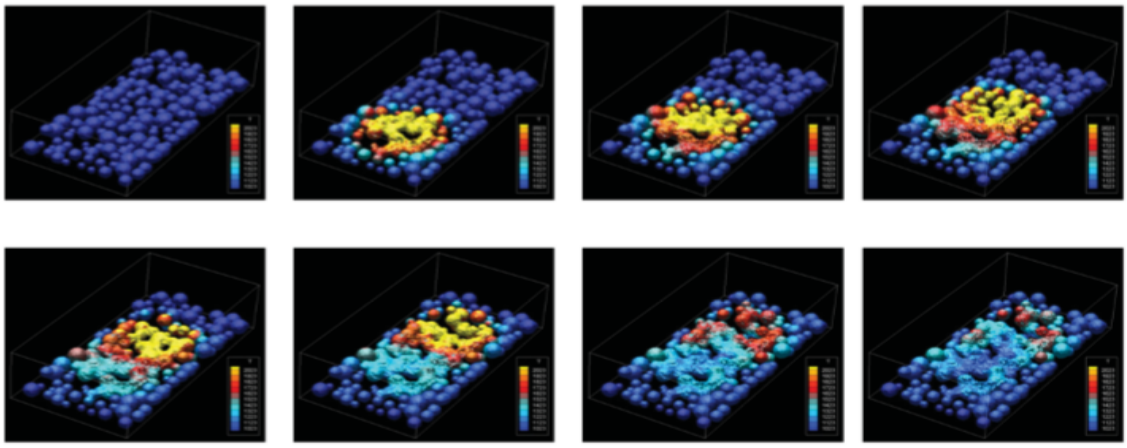

Figure 2-4: 3D Lattice-Boltzmann simulation of a 316L stainless-steel metal powder being melted by a 200W laser reproduced from [4]. It captures the phase transformation during the laser beam moving on a single scanning track. The color bar represent temperature. Yellow and red domain indicate melt pool .

layer in process. Another similar method is silent element method. Compared with element activation method, silent element method is a little different where all elements are active but the ones which are not supposed to be active have a very small conductivity and stiffness. Moreover, an adaptive mesh scheme is sometimes used to better capture the large temperature gradient close to the heat source. For example, Patil et al.(2015) [19] used an a dynamic mesh refinement that could move with the heat source.

The references using continuum models focus on two types of problems, the pure thermal field evaluation and thermal-mechanical response. Hodge et al.(2014) [5] build a fine mesh operating on melt pool geometry at overhanging areas and thermal-mechanical responses on a cube example in SLM process, the results for the latter one are shown in Fig. 2-5. Bo Cheng et al.(2016) [6] studied the influence of different scanning strategies on temperature distribution and residual stress and found that out-in strategy gives largest σ_{xx} and σ_{yy} stress while 45° line scanning case has the smallest σ_{xx} and σ_{yy} stress. Results for the temperature history are exhibited in Fig. 2-6. Reader is referred to in review article [8] for more examples. Also, it's good to see efforts have been made on reduce computational time in various aspects. Y.Yang et al.(2018) [20] introduced analytical results to help resolving large gradients occurring in the vicinity of the laser spot. Mercelis and Peters(2006) [21] built a simplified theoretical model based on the mechanism for residual stress and directly applied it on the stress prediction. Munro et al.(2019) [22] proved the feasibility of a on process-step parallel computational scheme from a pure mechanical perspective, which is much more efficient than conventional sequential layer-by-layer process simulation. However, these work either only pay attention to model simplification, or only focus on computational techniques. In our research we propose yet another simplified and hence fast thermo-mechanical model but our method is totally new in the AM process modelling literature. For model simplification, the heat load is assumed to be applied simultaneously on a whole surface. The scanning pattern is thus no longer resolvable in this macroscopic model. Furthermore, in stead of using element activation method or silent element method, the part growing is realized by element self-growing so that

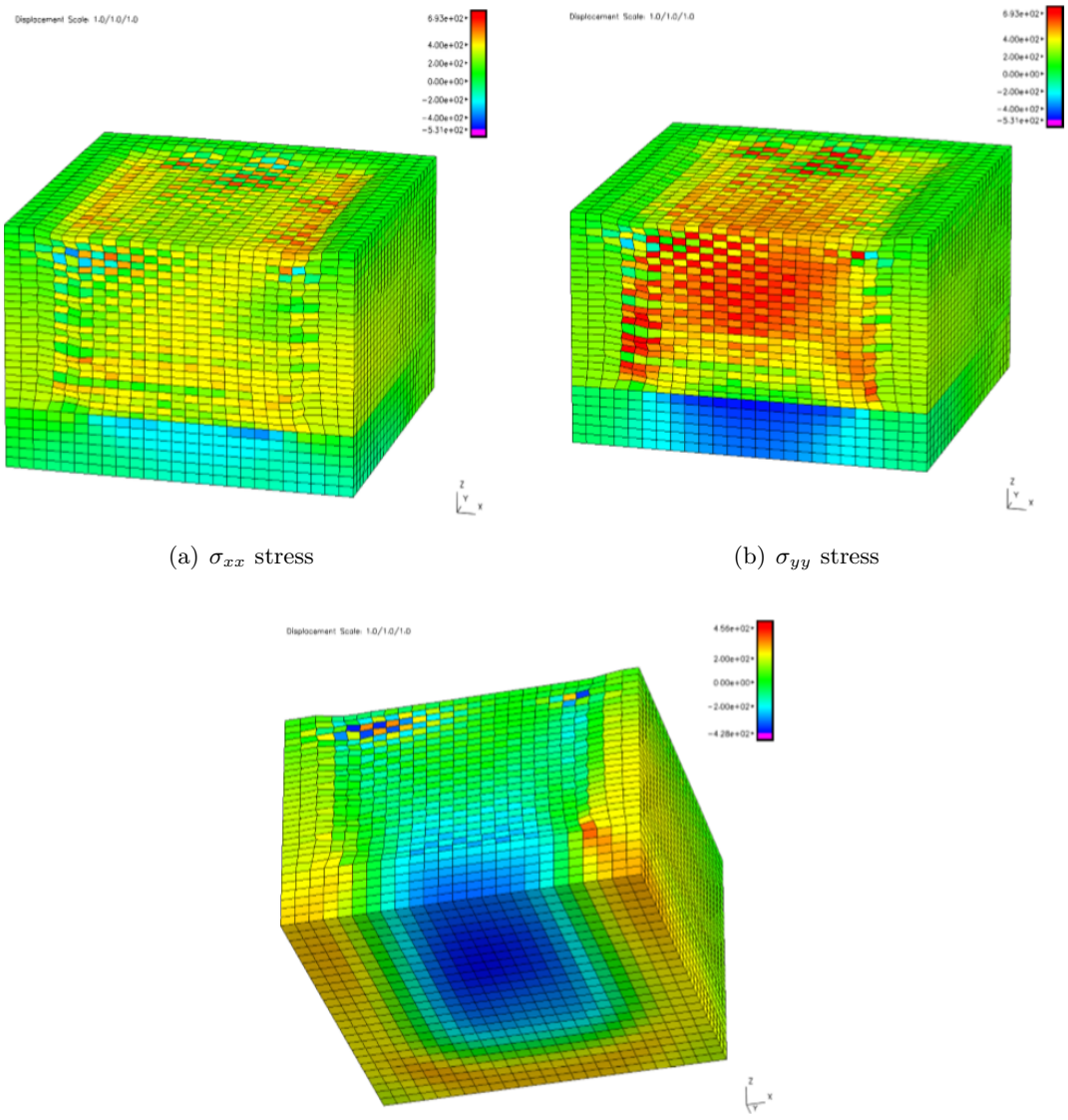

(a) σ_{xx} stress

(b) σ_{yy} stress

(c) σ_{zz} stress

Figure 2-5: Stress distribution [**MPa**] after 12 layers deposited within a cube reproduced from [5]. These figures are plotted with identical contour ranges. Compared with (a), (b) displays more extreme stresses in Y direction since there are less constraints in X direction. It also shows a strong gradient in stress between compression in the base plate and tension in the upper layers of consolidated materials. (c) illustrates the stresses in the Z direction. In particular, large compression can be seen in lower part of the cube and gradually drops to the lateral directions.

in each time step the total number of elements will remain the same. It's our anticipation that the part-scale model will dramatically reduces the computational time [15]. Although this time saving is achieved with the cost of losing part of the accuracy, it's neened to point out that the focus of part-scale model, it's not the local details of temperature and stress field, but the average evolution of these fields, and these information may give indications for

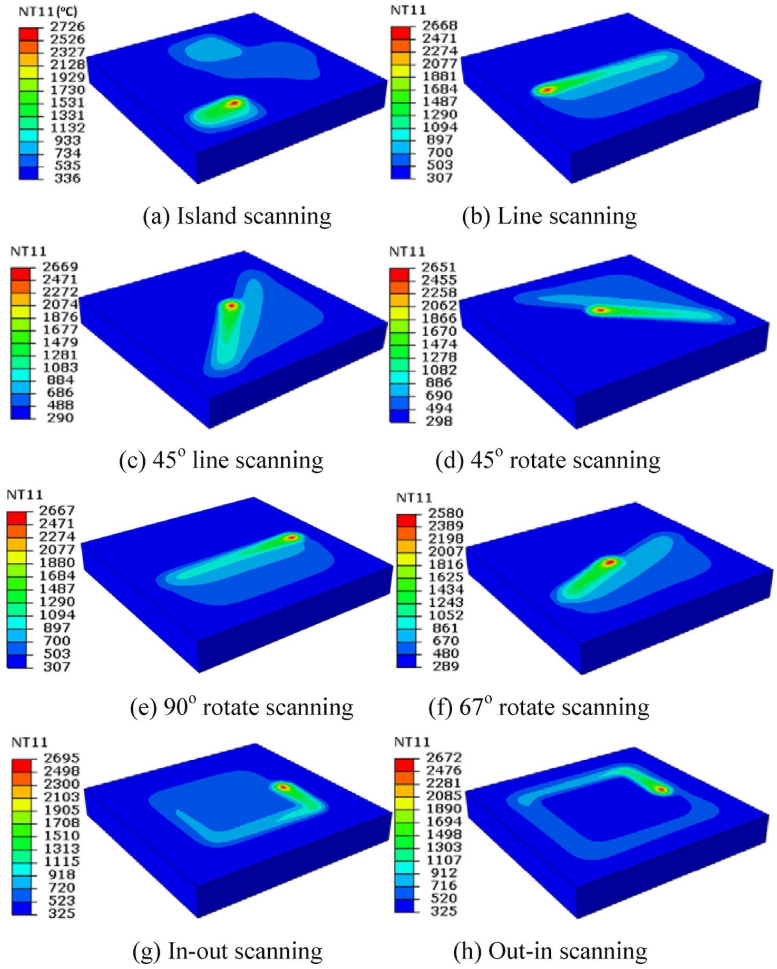

Figure 2-6: Tempreature distribution (NT11) with different scanning strategies [6]. It can be observed that the substrate temperature will not be room temperature during the scanning process. The 45° line scanning and 67° rotate scanning cases have relatively low substrate temperature while the maximum substrate temperature occurs in island scanning case since it takes longer time to complete a layer and more energy will be absorbed.

quality improvement with optimal process parameters. The main content of this part-scale moving mesh method will be introduced in Chapter 3 and Chapter 4, with Chapter 3 focusing on thermal analysis and Chapter 4 focusing on stress field.

Chapter 3

Part-scale thermal modelling

Even when excluding the most computational demanding hydrodynamics part, continuum process modeling of the AM process is computationally demanding. In order to further reduce the computational cost, it is assumed that the heat load is applied on the whole surface orthogonal to build direction and a single layer is built simultaneously instead of explicitly simulating laser scanning vectors. Furthermore, as mentioned in Chapter 2, the conventional way to deal with a growing domain in AM problems is the element activation technique, during which the number of elements keeps increasing with time. Consequently, the total number of elements, at the later stages of the simulation becomes computationally prohibitive. In order to reduce the computational costs, two measures are taken to make the simulation process more efficient. First, a part-scale approach is followed which simplifies the domain growth in a layer by layer fashion and the heat source associated. Apart from this, our moving mesh method provides a unique approach for mimicking this simplified domain growth while keeping the total number of elements fixed.

3-1 Model description

The simulation of powder bed fusion process consists of numerous heating and cooling cycles. During a heating stage, the powder is melted and fused which subsequently solidifies and hence the solid domain grows, while in a cooling stage the heat source is removed and a new powder layer is recoated. This phenomenon is repeated for each layer to be deposited. This characteristic feature of the powder bed fusion process inspires us to propose a model of the process based on this inherent domain growth and the associated special treatment of the thermal evolution of the part [23].

For the purpose of explaining the inherently growing nature, we start with a 1D case for simplicity with the well-known heat transfer equation,

$$\frac{\partial T}{\partial t} = \alpha \frac{\partial^2 T}{\partial y^2}. \tag{3-1}$$

In Eq. (3-1), T is the temperature field and α is the thermal diffusivity, y is the vertical

position and t is the time. During a heating stage of the AM process, the work piece is growing inside the build chamber, so the length of the domain l is increasing with time. We then assume material point with an initial coordinate y(t=0) moves in accordance with the growth rate of the domain, see Fig. 3-1. The left hand side of Eq. (3-1) then modified as:

$$\frac{\partial T\left(y\left(t\right),t\right)}{\partial t}=\alpha\frac{\partial^2 T}{\partial y^2}+\frac{\partial T}{\partial y}\frac{\partial y}{\partial t}. \tag{3-2}$$

The term $\partial y/\partial t$ in Eq. (3-2) is the local growth rate. In order to derive the expression for this term, consider the five evenly spaced material points and their evolution in response to domain growth in Fig. 3-1. Note that the local growth rate $\partial y/\partial t$ depends on the vertical position. Consequently, the growth rate at $y=l$ becomes $\dot{l}$ and the the growth rate of material

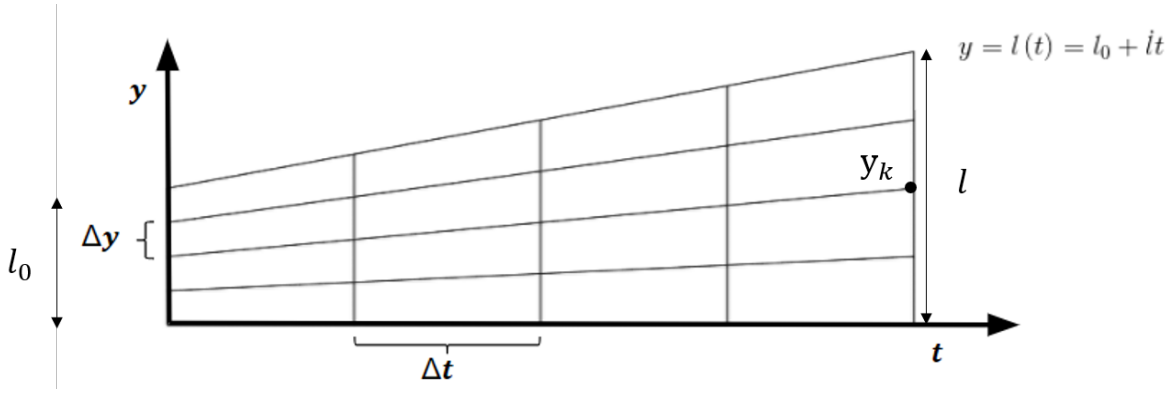

Figure 3-1: A 1D grid shows how vertical position of each node grows in time.

points below can be expressed as $y\dot{l}/l$. Consider now the evenly spaced material points to be grid points for spatial discretization of the domain. Therefore, an expression of growth rate for node k reads:

$$\left(\frac{\partial y}{\partial t}\right)_k=\frac{y_k}{l}\dot{l}, \tag{3-3}$$

where y_k is the position of node k. Now we substitute Eq. (3-1) into Eq. (3-2) and combine with Eq. (3-3). The governing equation during the heating stage in 1D can then be written as:

$$\frac{\partial T}{\partial t}=\frac{\partial T}{\partial y}\frac{y_k}{l}\dot{l}+\alpha\frac{\partial^2 T}{\partial y^2}. \tag{3-4}$$

For cooling stage, since the domain is stationery, $\dot{l}=0$. Eq. (3-4) thus simplifies to Eq. (3-1).

Now consider a two-dimensional part with an arbitrary shape built in a rectangular build chamber shown in Fig. 3-2 with a building direction coinciding with the positive y direction. The process begins with a base plate present at $t=0$. Base plate and work piece make up the solid domain. Observe that the part is in surrounded with powder. Now we denote the whole solid domain as Ω. $\partial\Omega_{\text{top}}$ is the top surface and $\partial\Omega_{\text{bot}}$ is the bottom surface. $\partial\Omega_{\text{lat}}$ is the lateral surface and $\partial\Omega_{\text{int}}$ is the interface between the solid work piece and the powder domain.

Fig. 3-2 also defines several important dimensions, in which w_0 is the width of the build chamber and l_0 is the thickness of base plate, l denotes the current combined thickness of the base plate and the work piece.

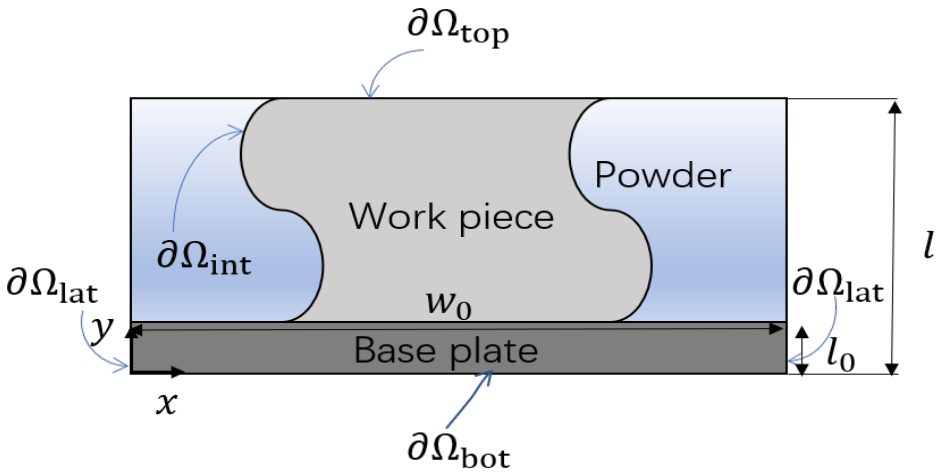

Figure 3-2: Model description for SLM process. Arbitrarily shaped work piece attached on a base plate and surrounded by powder domain. Boundaries and interfaces are also described. The dimensions in a build chamber are: w_0 is the width of the build chamber and l_0 is the thickness of base plate, l denotes the current combined thickness of the base plate and the work piece.

3-1-1 Boundary value problems

The 2D heat equation, to describe the temperature field T during a heating stage of Ω by taking into account the growing domain reads,

$$\frac{\partial T}{\partial t} = \frac{\partial T}{\partial y}\frac{y_k}{l}\dot{l} + \alpha\left(\frac{\partial^2 T}{\partial x^2} + \frac{\partial^2 T}{\partial y^2}\right), \tag{3-5a}$$

where the domain growth in the y direction is accounted for and since the width of the build chamber remains constant, no convective term appears with respect to x coordinate.

In order to determine the temperature development during a heating stage, we need to describe boundary conditions and an initial condition. For top surface $\partial\Omega_{\text{top}}$, the powder is assumed to be heated simultaneously. This phenomenon is mimicked by prescribing a Dirichlet boundary condition:

$$T = T_m, \text{ on } \partial\Omega_{\text{top}}, \tag{3-5b}$$

where T_m is the melting point for the material of interest. It is known that the heat conduction ability in powder is merely a small fraction of that of the solid, hence it is reasonable to neglect the heat conduction between solid domain and powder domain. The boundary no heat flux condition on $\partial\Omega_{\text{int}}$ is thus prescribed as,

$$\text{grad}T \cdot \mathbf{m} = 0 \ , \text{ on } \partial\Omega_{\text{int}}. \tag{3-5c}$$

$\mathbf{m}$ is unit outward vector on $\partial\Omega_{\text{int}}$. As for lateral surfaces, normally SLM process is performed in a closed build chamber. Consequently, adiabatic boundary conditions are deemed suitable on the lateral boundary surfaces as:

$$\text{grad}T \cdot \mathbf{n} = 0, \text{ on } \partial\Omega_{\text{lat}}. \tag{3-5d}$$

$\mathbf{n}$ is the unit outward vector on $\partial\Omega_{\text{lat}}$. The bottom surface of the base plate during the heating stage typically stays at a constant temperature, and the associated boundary condition reads:

$$T = T_0, \text{ on } \partial\Omega_{\text{bot}}, \tag{3-5e}$$

where T_0 is room temperature. Eventually the initial condition is given as:

$$T(x, y) = T_0, \text{ at } t = 0. \tag{3-5f}$$

This implies initially the whole base plate is at room temperature. Eq. (3-5) describes the boundary value problem to be solved during a heating stage.

During a cooling stage, the solid domain is stationery c.f. Eq. (3-1) and the heat load is temporarily removed from $\partial\Omega_{\text{top}}$. The associated governing equation with $\dot{l} = 0$ in 2D reads,

$$\frac{\partial T}{\partial t} = \alpha \left(\frac{\partial^2 T}{\partial x^2} + \frac{\partial^2 T}{\partial y^2} \right). \tag{3-6a}$$

In the absence of laser heating during a cooling stage, heat convection from the top surface becomes a prominent heat transfer mechanism. Therefore, the boundary condition on the top boundary is,

$$\mathbf{q} \cdot \mathbf{z} = h_c(T - T_0), \text{ on } \partial\Omega_{\text{top}}, \tag{3-6b}$$

where $\mathbf{z}$ is the unit outward vector on $\partial\Omega_{\text{top}}$, h_c is convection coefficient, T_0 is the temperature of the build chamber atmosphere assumed to be equal to room temperature and T is the instantaneous temperature on the top surface, while $\mathbf{q}$ denotes the heat flux lost from the top surface. The remaining thermal boundary conditions are identical to those we described for a heating stage are given as:

$$\text{grad}T \cdot \mathbf{m} = 0 \text{ , on } \partial\Omega_{\text{int}}, \tag{3-6c}$$

$$\text{grad}T \cdot \mathbf{n} = 0, \text{ on } \partial\Omega_{\text{lat}}, \tag{3-6d}$$

$$T = T_0, \text{ on } \partial\Omega_{\text{bot}}, \tag{3-6e}$$

and the initial condition is taken directly from the end of the previous heating step.

Up to now all the equations are defined in the $x - y$ space. In order to further simplify the governing equations, the following dimensionless transformations are introduced:

$$\theta = \frac{T - T_0}{T_m - T_0}, \tag{3-7a}$$

$$Y = y/l_0, \tag{3-7b}$$

$$X = x/w_0, \tag{3-7c}$$

$$H = l/l_0, \tag{3-7d}$$

$$\zeta = Y/H, \tag{3-7e}$$

$$\tau = \frac{t\alpha}{l_0^2}, \tag{3-7f}$$

$$\dot{H} = \frac{\partial H}{\partial \tau} = \frac{\dot{l}}{l_0}\frac{l_0^2}{\alpha} = \frac{\dot{l} l_0}{\alpha}, \tag{3-7g}$$

$$\beta = l_0 / w_0, \tag{3-7h}$$

$$Bi = \frac{h_c l_0}{k}. \tag{3-7i}$$

θ is the dimensionless temperature ranges from 0 to 1, Y is the dimensionless coordinate in the vertical direction and H is a dimensionless parameter indicates the instantaneous height for the solid domain with respect to the thickness of the base plate. X is the dimensionless coordinate in horizontal direction also ranges from 0 to 1.

The parameter ζ is defined as Y/H that ranges from 0 and 1. The growing domain in ζ space becomes a stationary domain and the position of the top surface is always fixed at $\zeta = 1$. The rest of the variables are τ that represents dimensionless time and β represent the aspect ratio of the base plate. $\dot{H}$ is the dimensionless growth rate which combines the effect of $\dot{l}$ and thermal diffusivity α that controls the domain growth rate in $X - \zeta$ space. Also, in Eq. (3-7i) the dimensionless Biot number is defined. Similar to the dimensionless parameter $\dot{H}$, dimensionless Biot number, which integrates thermal conductivity k and convection coefficient h_c, describes the possible influence on temperature evolution due to the material choice and the process conditions during the cooling stage.

We proceed to state the governing equation and boundary conditions valid for both heating and cooling stages in terms of dimensionless variables as,

$$\frac{\partial \theta}{\partial \tau} = \frac{\partial^2 \theta}{\partial \zeta^2}\frac{1}{H^2} + \frac{\partial \theta}{\partial \zeta}\frac{\zeta}{H}\dot{H} + \beta^2 \frac{\partial^2 \theta}{\partial X^2}. \tag{3-8a}$$

$$\theta = 1, \text{ on } \partial\Omega_{\text{top}}, \tag{3-8b}$$

$$\theta = 0, \text{ on } \partial\Omega_{\text{bot}}, \tag{3-8c}$$

$$\text{grad}\theta \cdot \mathbf{m} = 0 \ , \text{ on } \partial\Omega_{\text{int}}, \tag{3-8d}$$

$$\text{grad}\theta \cdot \mathbf{n} = 0, \text{ on } \partial\Omega_{\text{lat}}, \tag{3-8e}$$

$$\theta(X, \zeta) = 0, \text{ at } \tau = 0. \tag{3-8f}$$

The dimensionless form for equations in the cooling stage can be read as,

$$\frac{\partial \theta}{\partial \tau} = \frac{\partial^2 \theta}{\partial \zeta^2}\frac{1}{H^2} + \beta^2 \frac{\partial^2 \theta}{\partial X^2} \tag{3-9a}$$

$$\mathbf{Q} \cdot \mathbf{z} = \text{Bi}(\theta - \theta_0), \text{ on } \partial\Omega_{\text{top}}, \tag{3-9b}$$

$$\theta = 0, \text{ on } \partial\Omega_{\text{bot}}, \tag{3-9c}$$

$$\text{grad}\theta \cdot \mathbf{m} = 0 \ , \text{ on } \partial\Omega_{\text{int}}, \tag{3-9d}$$

$$\text{grad}\theta \cdot \mathbf{n} = 0, \text{ on } \partial\Omega_{\text{lat}}, \tag{3-9e}$$

and the initial conditions follow the results in the last step in the previous heating stage. in Eq. (3-9a) the convective term disappears by setting $\dot{H} = 0$ as the domain in cooing stage is not growing anymore. $\mathbf{Q}$ is the dimensionless heat flux from $\partial\Omega_{\text{top}}$ into the surrounding atmosphere.

In addition, the governing equation for an element activation method can also be derived using equations above with minor changes: dimensionless growth rate $\dot{H}$ vanishes and H value is always 1 since in element activation method we assume the building domain grows by adding new elements rather than element self-growing. The interval between nodes in vertical direction will be fixed but more nodes are added into the grid during the process.

3-1-2 Finite difference scheme

Compared with the classical 2D heat transfer equation valid for a fixed domain, the moving grid equation is slightly different because of the convective term. This category of equations are reminiscent to those used to solve free boundary problems in mathematics. A salient example of free boundary problems is the Stefan problem, which is raised by the Slovenian physicist Josef Stefan around 1890. Stefan problem is about the heat conduction or equivalently diffusion in a two phase system where the interface between the phases moves, for instance, freezing or melting problems and gas-solid reactions [24, 25].

In 1987, Crank [26] developed several finite difference schemes for solving moving boundary problems (MBP) in his book. The numerical solution directly based on Eq. (3-5a) is called front tracking method since the boundary keeps moving. After the dimensionless transformation, Eq. (3-8a) describes a fixed domain in the $X-\zeta$ space and the solution based on this boundary immobilization of the grid is called front-fixed methods [27]. The distinction between SLM process modelling and the Stefan problem is the way to determine convective term. In Stefan problem, the boundary growth rate is governed by the heat balance at the interface while in SLM process, the growth rate is an input parameter and it is determined depending on part geometry and printing conditions.

The finite difference mesh, which is shown in Fig. 3-3, illustrates how the grids evolve in both front tracking scheme and front-fixed scheme. Fig. 3-3 (a) Fig. 3-3 (b) show the progression of a front-tracking grid in $x-y$ space from time step i to time step $i+1$. The front-fixed grid in $X-\zeta$ space is illustrated in Fig. 3-3 (c) and Fig. 3-3 (d). For front-tracking scheme, Δx, Δy indicate discretization size on x and y direction, $T^{i}_{m,n}$ indicates the temperature value for node located at $(m\Delta x, n\Delta y)$ at time step i, while $T^{i+1}_{m,n}$ indicates the nodal temperature for the same node at time step $i+1$. In the front-fixed grid, ΔX and $\Delta\zeta$ are the dimensionless discretization size in $X-\zeta$ space, t is replaced by dimensionless time unit τ. Nodal temperature is represented by a dimensionless quantity θ defined as the ratio between difference of current nodal temperature T and room temperature T_0, versus the difference of metal melting temperature T_m and room temperature T_0. The element growth can be noticed in the front-tracking grid, but for the front-fixed scheme, the top boundary will always remain stationary at $\zeta=1$ during the time evolution and a square mesh is thus established via dimensionless transformation.

Recalling that for X and ζ, their ranges are both from 0 to 1, then the advantage for building front-fixed grid is that if the node number is equally assigned, it can be ensured the grid points are evenly spaced in X and ζ axes, which gives $\Delta X=\Delta\zeta$. It is therefore suggested to derive the finite difference scheme for the heating stage based on a front-fixed grid shown in Fig. 3-3 (c) and Fig. 3-3 (d).

If a node is located on $\partial\Omega_{\text{top}}$, its temperature will be

$$\theta^{i+1}_{m,n}=1, \tag{3-10a}$$

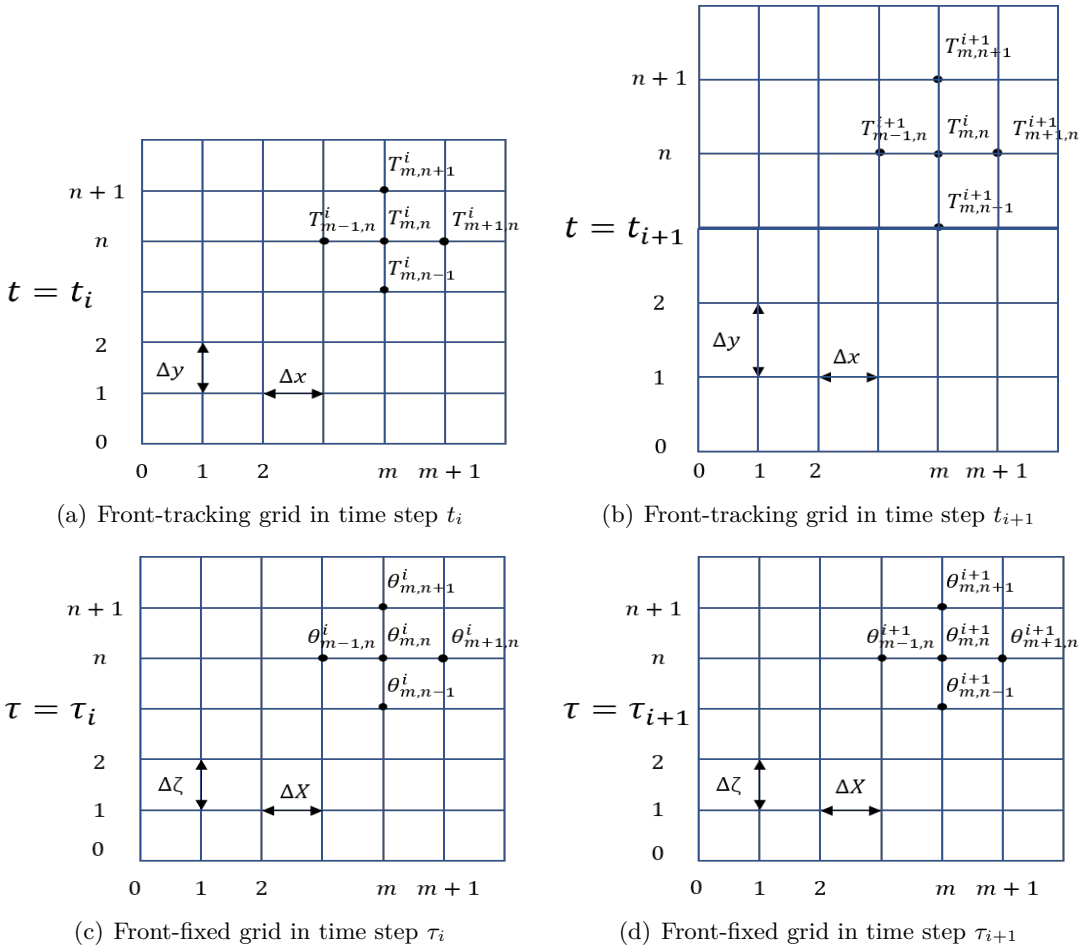

(a) Front-tracking grid in time step t_i

(b) Front-tracking grid in time step t_{i+1}

(c) Front-fixed grid in time step τ_i

(d) Front-fixed grid in time step τ_{i+1}

Figure 3-3: Illustration for 2D finite difference grid. (a) and (b) present grid evolution for a front-tracking grid from time step t_i to t_{i+1}. (c) and (d) depict the front-fixed mesh at time step τ_i to τ_{i+1}. It can be seen that the top boundary remains stationery and the intervals between nodes are identical.

where $\theta^{i+1}_{m,n}$ indicates the dimensionless temperature at the position $(m\Delta X, n\Delta\zeta)$ at time τ_{i+1}. For node on the bottom surface of the base plate $\partial\Omega_{\text{bot}}$, the nodal temperature expression is,

$$\theta^{i+1}_{m,n} = 0. \tag{3-10b}$$

When it comes to $\partial\Omega_{\text{lat}}$, the discretization boundary reads as,

$$\frac{\theta^{i+1}_{m,n} - \theta^{i+1}_{m+1,n}}{\Delta X} = 0, \text{ on left side, or } \frac{\theta^{i+1}_{m,n} - \theta^{i+1}_{m-1,n}}{\Delta X} = 0, \text{ on right side,} \tag{3-10c}$$

where ΔX is dimensionless nodal spacing in the horizontal direction. There are two equations as the former one is for the left side and the latter one is for the right side. The boundary condition on $\partial\Omega_{\text{int}}$ is expressed as,

$$\frac{\theta^{i+1}_{m+1,n} - \theta^{i+1}_{m-1,n}}{\Delta X} = 0, \text{ or } \frac{\theta^{i+1}_{m,n+1} - \theta^{i+1}_{m,n-1}}{\Delta\zeta} = 0, \tag{3-10d}$$

where $\Delta\zeta$ is another dimensionless nodal spacing in building direction. These two equations also set the temperature for the powder nodes that surround the interface nodes.

Eventually, for the interior grid points, the finite difference equation centered in space forward in time to update nodal temperature is given as,

$$\begin{aligned}\theta_{m,n}^{i+1} = &\frac{\Delta\tau}{\Delta\zeta^2}\left(\theta_{m,n+1}^{i} - 2\theta_{m,n}^{i} + \theta_{m,n-1}^{i}\right)\frac{1}{H^2} + \frac{\Delta\tau}{2\Delta\zeta}\left(\theta_{m,n+1}^{i} - \theta_{m,n-1}^{i}\right)\dot{H}\frac{\zeta}{H} \\ &+ \beta^2\frac{\Delta\tau}{\Delta X^2}\left(\theta_{m+1,n}^{i} - 2\theta_{m,n}^{i} + \theta_{m-1,n}^{i}\right) + \theta_{m,n}^{i}\end{aligned} \tag{3-10e}$$

where $\Delta\tau$ is the dimensionless time step. Recall that, $\dot{H}$ is the dimensionless growth rate. $\theta_{m,n}^{i}$ is the dimensionless temperature value for the node in position $(m\Delta X, n\Delta\zeta)$ at current time step i and $\theta_{m,n}^{i+1}$ is the nodal temperature at the same position at time step $i+1$.

Eq. (3-10a), Eq. (3-10b) and Eq. (3-10e) seem quite straightforward to understand, for Eq. (3-10c) and Eq. (3-10d), detailed explanation is sketched in Fig. 3-4.

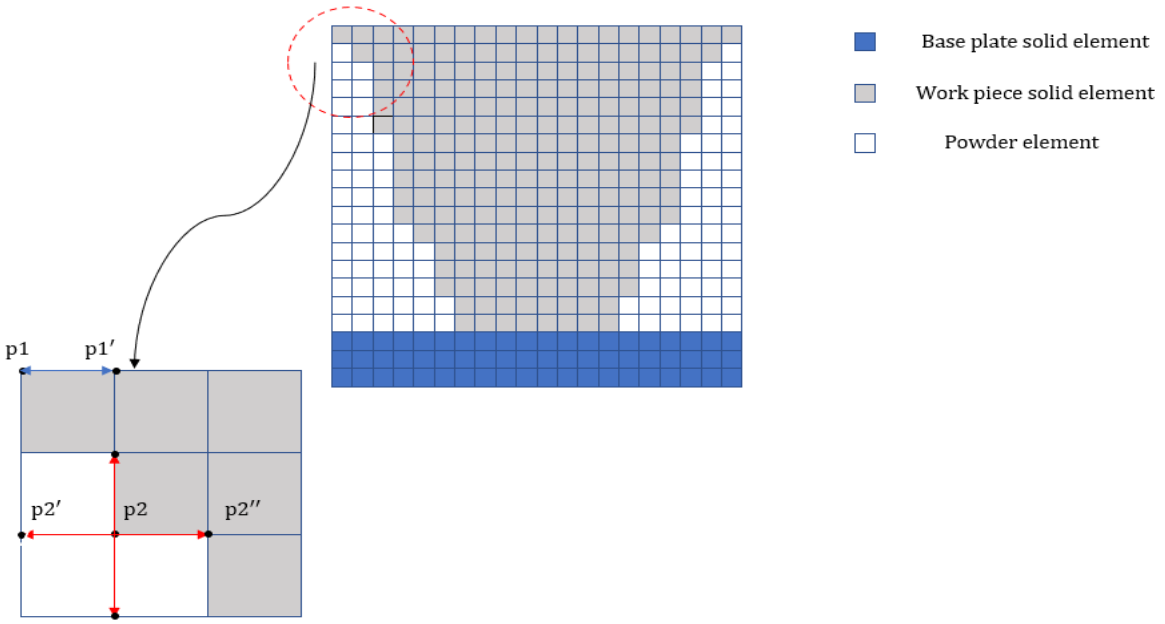

Figure 3-4: Illustration for heat boundary conditions on both sides. If a node is located on the boundary of build chamber, then in every time step the nodal temperature is updated as the temperature value of the node next to it in the horizontal direction. If a node is on the interface, we first deal with the nodes around it and subsequently the interface node is updated as an internal node.

Suppose a mesh is built like depicted in Fig. 3-4 and temperature value on the lateral boundary or interface need to be determined. According to the insulated boundary condition on the lateral surface, the temperature of a solid boundary node will be equal to the temperature of the solid node next to it in the horizontal direction. For example, for solid boundary node $p1$ shown in Fig. 3-4, its value will be assigned as equal to the value of point $p1'$ and these two points are connected by a double blue arrow.

For solid nodes fall on the interface, where again an insulated heat boundary condition is applied. Due to the choice of the structured grid, the solid-powder interface is reminiscent of a staircase. Hence a single solid interface node will be surrounded by four other nodes. If a powder node is found around the interface node, the temperature of powder node will be first assigned to be equal to the temperature of the nearest solid node (not the interface one) on the same straight line. For instance, the temperature of powder point $p2'$ will be set equal to the temperature of solid node $p2''$. Interface node $p2$, powder node $p2'$ and solid node $p2''$ are on the same straight line. By doing so, the temperature value for powder nodes around the interface node are given and thus the temperature value for the interface node can be calculated with Eq. (3-10e).

During the cooling stage, the discretization form for convective boundary condition on $\partial\Omega_{\text{top}}$ is expressed as:

$$\begin{aligned}\theta_{m,n}^{i+1} = &-\frac{2}{H^2}\frac{\Delta\tau}{\Delta\zeta^2}\left(\theta_{m,n}^{i} - \theta_{m,n-1}^{i}\right) + 2\text{Bi}\frac{\Delta\tau}{H\Delta\zeta}\left(\theta_e - \theta_{m,n}^{i}\right) + \\ &\beta^2\frac{\Delta\tau}{\Delta X^2}\left(\theta_{m+1,n}^{i} - 2\theta_{m,n}^{i} + \theta_{m-1}^{n}\right) + \theta_{m,n}^{i},\end{aligned} \tag{3-11a}$$

where Bi is dimensionless Biot number defined in Eq. (3-7i). θ_e is the temperature of the protective gas in the build chamber which equals to θ_0. The boundary condition on $\partial\Omega_{\text{bot}}$ is identical as in the heating stage:

$$\theta_{m,n}^{i+1} = 0. \tag{3-11b}$$

Boundary conditions on $\partial\Omega_{\text{lat}}$ and $\partial\Omega_{\text{int}}$ are also unchanged as,

$$\frac{\theta_{m,n}^{i+1} - \theta_{m+1,n}^{i+1}}{\Delta X} = 0, \text{ on left side, or } \frac{\theta_{m,n}^{i+1} - \theta_{m-1,n}^{i+1}}{\Delta X} = 0, \text{ on right side,} \tag{3-11c}$$

and,

$$\frac{\theta_{m+1,n}^{i+1} - \theta_{m-1,n}^{i+1}}{\Delta X} = 0, \text{ or } \frac{\theta_{m,n+1}^{i+1} - \theta_{m,n-1}^{i+1}}{\Delta\zeta} = 0. \tag{3-11d}$$

Finally, for nodes within the solid domain are updated as,

$$\begin{aligned}\theta_{m,n}^{i+1} = &\frac{\Delta\tau}{\Delta\zeta^2}\left(\theta_{m,n+1}^{i} - 2\theta_{m,n}^{i} + \theta_{m,n-1}^{i}\right)\frac{1}{H^2} + \beta^2\frac{\Delta\tau}{\Delta X^2}\left(\theta_{m+1,n}^{i} - 2\theta_{m,n}^{i} + \theta_{m-1,n}^{i}\right) \\ &+ \theta_{m,n}^{i}.\end{aligned} \tag{3-11e}$$

3-1-3 Stability condition

The explicit finite difference scheme shows superiority in computational speed because no matrix inversion is involved, and its concise format also makes it easy to implement for numerical simulation. However, a major drawback of the explicit finite difference method is that the allowable size of the time step is limited by stability requirements. To avoid the divergent oscillations in solution, the stability requirements for moving grid method will be discussed below.

There will be two stability conditions governing both horizontal and vertical direction for the moving grid scheme. For the heating stage, the horizontal stability condition can be expressed as:

$$\Delta t \leq \frac{\Delta x^2}{2\alpha}. \tag{3-12}$$

Eq. (3-12) is defined in $x-y$ space, by substituting Eq. (3-7c) and Eq. (3-7f) the stability condition in $X-\zeta$ space can be rewritten as:

$$\Delta\tau \leq \frac{\Delta X^2}{2\beta^2}. \tag{3-13}$$

In the ζ direction, because of the convective term, the requirement is given according to the result of S.Kutluay et al.(1995) [28] and the Von Neuman stability analysis [29]:

$$\Delta\tau < \frac{2\Delta\zeta^2}{\frac{4}{H^2} + \left(\Delta\zeta\dot{H}\right)^2}. \tag{3-14}$$

Eq. (3-13) can also represent the stability condition in the horizontal direction for the cooling stage since horizontal heat conduction is the same in both heating and cooling stage. For ζ direction during the cooling stage, $\dot{H}=0$ since the grid stops growing in the cooling stage, then the stability condition becomes:

$$\Delta\tau < \frac{\Delta\zeta^2}{2}H^2. \tag{3-15}$$

3-1-4 Finite difference grid

The spatial grid size and time step size are connected by the finite difference stability conditions. Once the grid size is fixed then the time step size can be determined.

In our model, the simulation begins when $l=l_0$, which corresponds to $H=1$ in $X-\zeta$ space. Moreover, we further set the final thickness of the part to be $l=4l_0$, which suggests the work piece thickness is $3l_0$ and corresponding to $H=4$ in $X-\zeta$ space.

Frazier et al. (2014) [1] concluded the build in volume of mainly used SLM machines, the value for base plate width w_0 and thickness l_0 can be assigned as $w_0=0.1$ m and $l_0=0.01$ m.

A reasonable spatial discretization can be found by referring the value of layer thickness. In SLM process, the layer thickness is between 30 μm to 100 μm [8]. In the simulation, the layer thickness is selected to be 50 μm. Based on the value for l_0, it can be calculated that the base plate is equivalent to 200 layers and work piece requires 600 layers for completion. If 26 grid points are introduced in both directions, then the grid accommodates a total of 676 grid points which form 625 square elements. In building direction, there will be 8 layers contained in a single element in the beginning and 32 at the end of the process, which is an acceptable value for a part scale model. The spatial grid size is computed by referring the defined node number. In $X-\zeta$ space, ΔX and $\Delta\zeta$ are both equal to 0.04.

If Inconel 718 is chosen for the simulation with the dimensionless grow rate $\dot{H}=0.0008$, then total heating time (dimensionless) for the whole process is $\tau=\frac{4-1}{\dot{H}}=3000$. Consequently, the time discretization size is determined by the stability requirements:

$$\Delta\tau \leq \frac{\Delta X^2}{2\beta^2} = 0.08, \tag{3-16a}$$

$$\Delta\tau \leq \frac{2\Delta\zeta^2}{4+\left(\Delta\zeta\dot{H}\right)^2} \approx 0.0008. \tag{3-16b}$$

It is thus the time step size $\Delta\tau$ for Inconel 718 can be chosen as 6×10^{-4}. Depending on the value of $\Delta\tau$, the minimum number of total time steps, $nt = \tau/\Delta\tau$, is 5×10^6. These value for total time step n_t is also feasible for the other two materials after stability checking, but $\Delta\tau$ value will depend on corresponding $\dot{H}$ value.

During the domain growth process, grid points that are representing a solid material point might end up on powder domain. Therefore, the property of the elements monitored at each time step. Elements with all four grid points are solid. Since our grid grows in time, during every time step, all the elements status will be checked and updated. Some example meshes can be seen in Fig. 3-5.

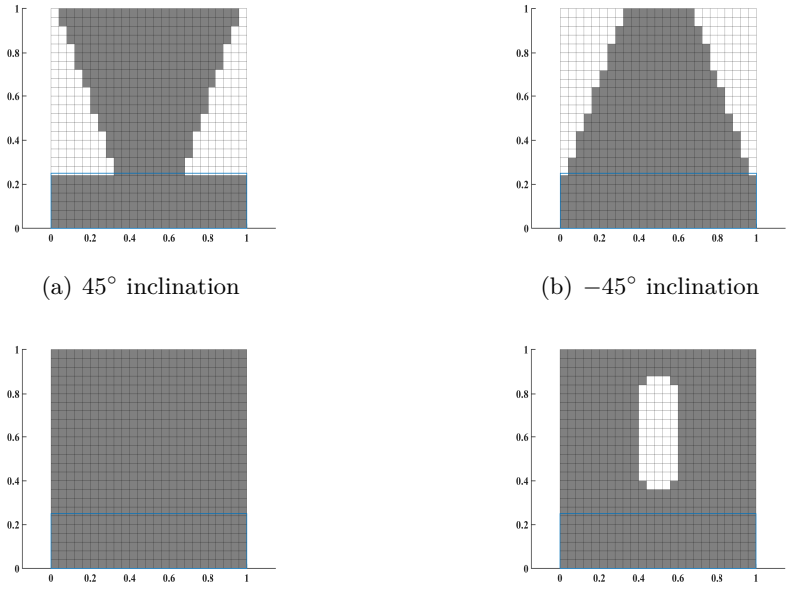

(a) 45° inclination

(b) −45° inclination

(c) Rectangle work piece

(d) Rectangle with a hollow out

Figure 3-5: Mesh building for work piece in different shape. The part surrounded by blue rectangle is the base plate. (a) $\gamma = 45°$. (b) $\gamma = -45°$. (c) $\gamma = 90°$. (d) geometry with a hole.

Actually a finer mesh is feasible with respect to modelling the part geometry, when element number in the mesh is increasing, a higher resolution for inclination contour can be achieved. However, the improvement in mesh resolution is at the cost of computational efficiency. For instance, if a mesh with 51 nodes in both building direction and horizontal direction, at least 30000000 time steps are required according to that stability condition. It is therefore almost 6 times increase in the computational time. The selection between mesh resolution and time cost is always a trade off. Regarding the huge computational burden brings by increasing the element number, a coarser mesh is preferred during the simulation.

3-2 Part geometry

Recall that in Section 3-1-1, a 2D model with an arbitrary shape is defined. However, concerning the part geometry for simulations, rectangle and trapezoids are considered for simplicity.

Fig. 3-6 shows a rectangular geometry: all the powder domain in work chamber will finally become solid when the process is over and in this case the surface $\partial\Omega_{\text{int}}$ coincides with surface $\partial\Omega_{\text{lat}}$.

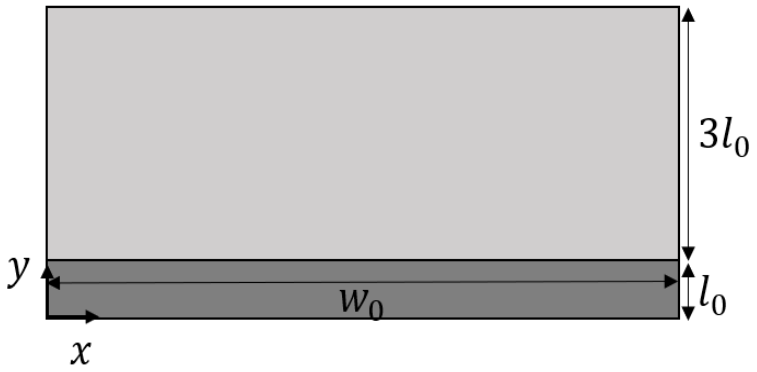

Figure 3-6: Illustration for rectangular geometry. The simulation begins with a base plate $l = l_0$, and ends up with a height $l = 4l_0$.

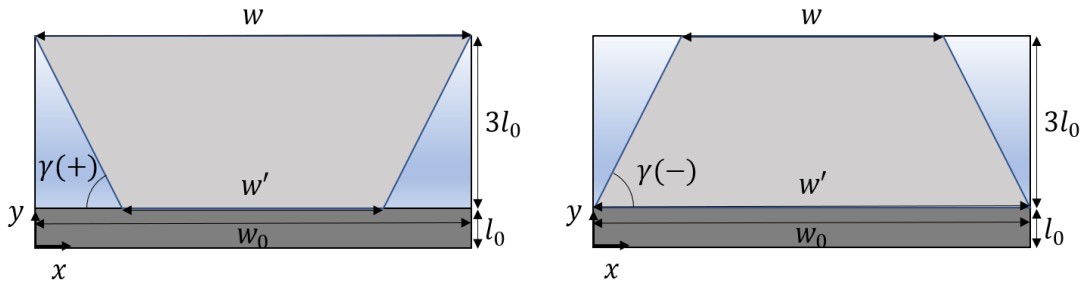

(a) Work piece with positive inclination

(b) Work piece with negative inclination

Figure 3-7: Work piece with an inclination. (a) If work piece top side is longer than work piece bottom side, then it is a positive inclination (b) If work piece top side is shorter than work piece bottom side, then it is a negative inclination.

Fig. 3-7 depicts the trapezoid work piece. An inclination γ is defined to adjust the shape of the trapezoid. w is the top side length of the trapezoid work piece and w' denotes the bottom side length of the work piece. The negative inclination γ in a trapezoid is when its bottom side length is longer than the top side length, i.e. $w > w'$, shown in Fig. 3-7 (b). In contrast, the trapezoid in Fig. 3-7 (a) suggests $w < w'$, which is a positive inclination.

7 different γ values are considered in this study. These inclinations are $\pm 45°$, $\pm 60°$, $\pm 75°$ plus $90°$ which is the rectangular case. The rule to switch between different inclinations are illustrated in Fig. 3-8: the length of the long side is unchanged (equals to w_0), and expand or reduce the length for the short side. A rectangle work piece is built when the top side length is equal to bottom side length. Illustrations are in Fig. 3-8.

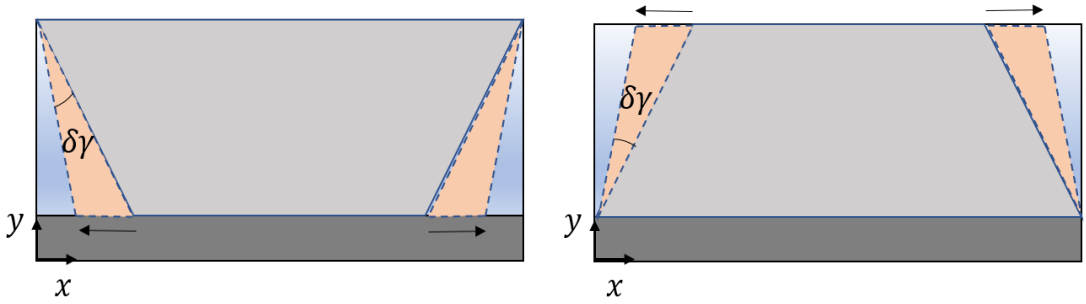

(a) Changing inclination (positive) (b) Changing inclination (negative)

Figure 3-8: Illustrations for how to change inclination in part geometry. (a) For positive angles, top side length is unchanged and bottom side length can be stretched (or reduced). (b) For negative angles, bottom side length is unchanged and top side length can be stretched (or reduced).

3-3 Process conditions and parameters

In this section, a thorough discussion will be carried out focusing on specific details of model variables including material properties and other process parameters. The meaning of these variables and how they are accounted for in the model are explained.

3-3-1 Growth rate

The dimensionless growth rate describes how fast the work piece height (H) grows in $X-\zeta$ space during SLM process simulation. Recall that $\dot{H} = \dot{l}l_0/\alpha$, $\dot{l}$ is the printing speed. In general, this value is given as a volumetric speed, but in Eq. (3-17) a linear speed is needed. The formula to calculate such a linear speed from volumetric speed is,

$$\dot{l} = \frac{v}{A}, \tag{3-17}$$

in which v denotes the volumetric printing speed and A is the cross section area from the top view of the work piece. In order to describe this cross section area A, a constant d_0 is defined to represent the out of plane dimension, i.e. the depth. A reasonable depth value can be taken as $d_0 = 0.1$ m. Therefore, the cross sectional area A for a rectangle work piece can be calculated as $A_0 = d_0 w_0 = 0.01$ m^2.

Three frequently used SLM materials are selected for the simulations, which are Inconel 718, 316L stainless steel and Ti-6Al-4V. The machine printing speeds are representative for of M2 Series 5 which is produced by GE additive. Recall that $\dot{H} = \dot{l}l_0/\alpha$ and typical $\dot{H}$ value corresponding to different materials for a rectangular work piece are thus calculated and listed out in Table 3-1.

However, when a trapezoid work piece is built, the $\dot{H}$ value will change during the process because of the varying in top cross sectional area. Accordingly, the relation between the dimensionless growth rate and the top cross sectional area can be written down as,

$$\frac{\dot{H}_0}{\dot{H}} = \frac{A_0}{A} = \frac{w_0 d_0}{wd}. \tag{3-18}$$

Table 3-1: Dimensionless growthrate values depending on material properties for rectangular work piece.

Material	Melting point(°C)	Conductivity (W/m · K)	Thermal diffusivity(m^2/s)	Printing speed(cm^3/h)	$\dot{H}$
316L	1380 [30]	34.39 [30]	7.22×10^{-6} [30]	21.9 [31]	8.42×10^{-4}
Inconel 718	1300 [32]	27.02 [33]	5.38×10^{-6} [33]	21.6 [31]	1.12×10^{-3}
Ti-6Al-4V	1630 [32]	25.96 [34]	5.68×10^{-6} [34]	40.4 [31]	1.98×10^{-3}

* Data for melting point and thermal diffusivity are collected from bulk material. The value of thermal diffusivity is evaluated at melting temperature.

For trapezoid examples depicted in Fig. 3-7, it can be seen that the work piece width varies with time and we assume depth is fixed, i.e. $d = d_0$, hence Eq. (3-18) is rewritten to describe both positive inclinations and negative inclinations.

$$\dot{H} = \frac{\dot{H}_0}{1 - 2\beta \tan\gamma\,(H - 1)} \tag{3-19a}$$

$$\dot{H} = \frac{\dot{H}_0}{1 - 2\beta \tan\gamma\,(H - 4)} \tag{3-19b}$$

γ in both of the equations means the inclination of the trapezoid work piece. Eq. (3-19a) is used for the negative inclination and Eq. (3-19b) is for the positive inclination. H value will keep updating as the grid grows and $\dot{H}_0$ here represents the value for $\dot{H}$ when the work piece top cross sectional area equals $A_0 = d_0 w_0$.

It can be concluded that the trapezoid inclination makes dimensionless grow rate $\dot{H}$ becomes a function of top cross sectional area, which further relies on current work piece thickness H. Recall that the pre-set value of the geometry parameters are $d_0 = 0.1$ m, $w_0 = 0.1$ m, if $\dot{H}_0$ is taken as 0.001, Eq. (3-19a) and Eq. (3-19b) are thus plotted for all 7 trapezoid inclination options in Fig. 3-9.

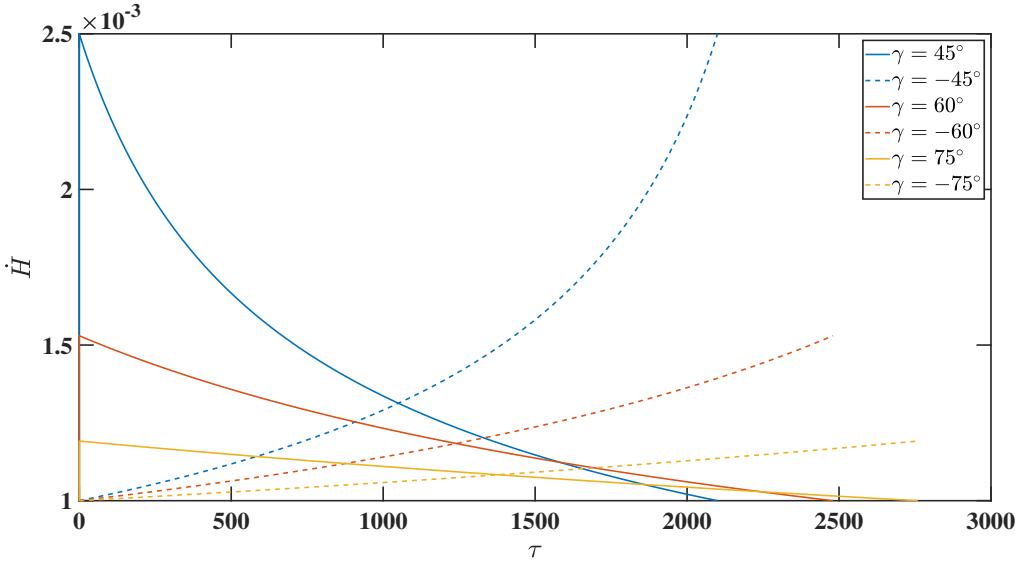

Figure 3-9: $\dot{H}$ evolution due to trapezoid inclinations during simulation(only contains heating steps). $\dot{H}_0 = 0.001$.

Fig. 3-9 displays that $\dot{H}$ curves for $\pm\gamma$ always intersect at some point. The work piece with an acute angle always shows a larger growth rate value because a small $|\gamma|$ value results in a limited top cross sectional area in the process. This growth rate variance for different γ also directly reflects on the duration of the heating/cooling cycle.

3-3-2 Cooling condition

As discussed earlier, a layer deposition in the SLM process comprises a heating stage and a cooling stage. During the cooling stage, the work piece is cooled down by heat convection in a protective gas atmosphere. The convection coefficient and cooling time are hence crucial in the cooling stage.

Biot number Bi is an integrated parameter combines thermal conductivity k and convection cooling coefficient h_c. Its value depends on both a material property and convection condition. Furthermore, a connection can be built between Biot number Bi and dimensionless grow rate $\dot{H}$ since $\dot{H}$ relies on thermal diffusivity α and $\alpha = k/(\rho c_p)$. This implies, $\dot{H}$ and Bi are not independent from each other. However, Biot number can be changed independent of $\dot{H}$ by means of changing h_c only, which represents the degree of convective cooling while keeping k constant. It is assumed that the convection type in build chamber is natural convection by air and the corresponding convection coefficient can be picked as 1 $\mathrm{W}\,(\mathrm{m}^2 \cdot \mathrm{K})$, 5 $\mathrm{W}\,(\mathrm{m}^2 \cdot \mathrm{K})$ and 10 $\mathrm{W}\,(\mathrm{m}^2 \cdot \mathrm{K})$ [35].

The cooling time, i.e. the duration of a cooling stage, is another critical parameter that influences work piece temperature distribution. This factor is evaluated by introducing a ratio between total heating time and total cooling time, written as λ. When $\lambda > 1$ means the heating stage is longer than the cooling stage. Generally in a SLM process, a heating stage should be considered more extended than the cooling stage, hence the λ values are selected as 6, 2 and 1. Additionally, the cooling duration in each heating/cooling cycle should also depend on the scanning area, hence the actual cooling time in each cycle is distributed according to the heating time in the same heating/cooling cycle.

3-4 Part scale simulation

There are four parameters that can fully define the SLM process. They are dimensionless growth rate $\dot{H}$, work piece geometry γ, heating/cooling time ratio λ and the last one is Biot number Bi. During the simulation, different combinations of process conditions and materials can be completely tested with these four parameters listed in Table 3-2.

Furthermore, mesh constants and dimensional parameters defined are listed in Table 3-3.

With all the conditions and parameters defined, the simulation flow chart can be plotted in Fig. 3-10. In the pre-processing part, the value of dimensionless grow rate, Biot number and heating/cooling time ratio that define process conditions and material properties are chosen. In the mesh scheme part, the work piece inclination controlling the shape of work piece is imported and the mesh is thus established. The appropriate thermal boundary conditions are applied depending on whether a heating stage or a cooling stage is simulated. A counter is set to check whether the heating stage is finished. If a layer is completely deposited, a cooling stage begins afterwards with another cooling counter to record the cooling time set by λ in

Table 3-2: As-used process conditions and simulation parameters

Parameter	value
$\dot{H}^*$	0.0008, 0.001,0.002
Bi *	1.850×10^{-3}, 2.908×10^{-4}, 1.454×10^{-3}, 5.816×10^{-3}
Inclination γ (°)	$-45°$, $-60°$, $-75°$, $90°$, $45°$, $60°$, $75°$
Heating/cooling cycle ratio λ	6, 2, 1

* Three types of materials (316L, Inconel 718, Ti-6Al-4V) will be used in the simulation. For simplicity, the approximate $\dot{H}$ value are taken from Table 3-1 .
* Bi is calculated based on the thermal conductivity of Inconel 718 and 316L.

Table 3-3: Mesh constants and dimension parameters

Constant	Meaning	Value
nx	number of nodes in horizontal direction	26
ny	number of nodes in vertical direction	26
Δx	spatial mesh size in horizontal direction($x-y$ space)	4×10^{-2} m
Δy	spatial mesh size in vertical direction($x-y$ space)	4×10^{-3} m
l_0	original length in vertical direction	0.01 m
w_0	length in horizontal direction	0.1 m
d_0	length in longitudinal direction	0.1 m
ΔX	spatial mesh size in horizontal direction($X-\zeta$ space)	0.04
$\Delta\zeta$	spatial mesh size in vertical direction($X-\zeta$ space)	0.04
nt^*	total time step in the simulation	5×10^6

* The time step size $\Delta\tau$ relies on $\dot{H}$ since $\Delta\tau = \tau/nt$ and $\tau = (4-1)/\dot{H}$. Also, when a trapezoid work piece is building, the total time step needed will be lower than 5×10^6, so the termination requirement of the simulation is to check the thickness of the work piece.

the pre-processing stage. When a cooling stage is completed, the termination condition will be examined to see whether the part geometry is completely built. Once the simulation is finished, the temperature data will then be saved for plotting, if the part geometry is still in processing, a new layer is deposited and the whole procedure repeats.

3-5 Result and discussion

The factors that influence temperature distribution can be attributed to four different aspects, which are part geometry defined by γ, heating/cooling time ratio λ, dimensionless grow rate $\dot{H}$ and Biot number Bi. In order to get an insight on how these parameters will have an impact on temperature field, for each parameter, a series of simulations are carried out. The parameter values are picked from Table 3-2 and simulation data will be recorded for discussion.

A useful parameter to quantify the temperature plot is the average value. In each time step, the average temperature can be defined as the temperature value for the whole work

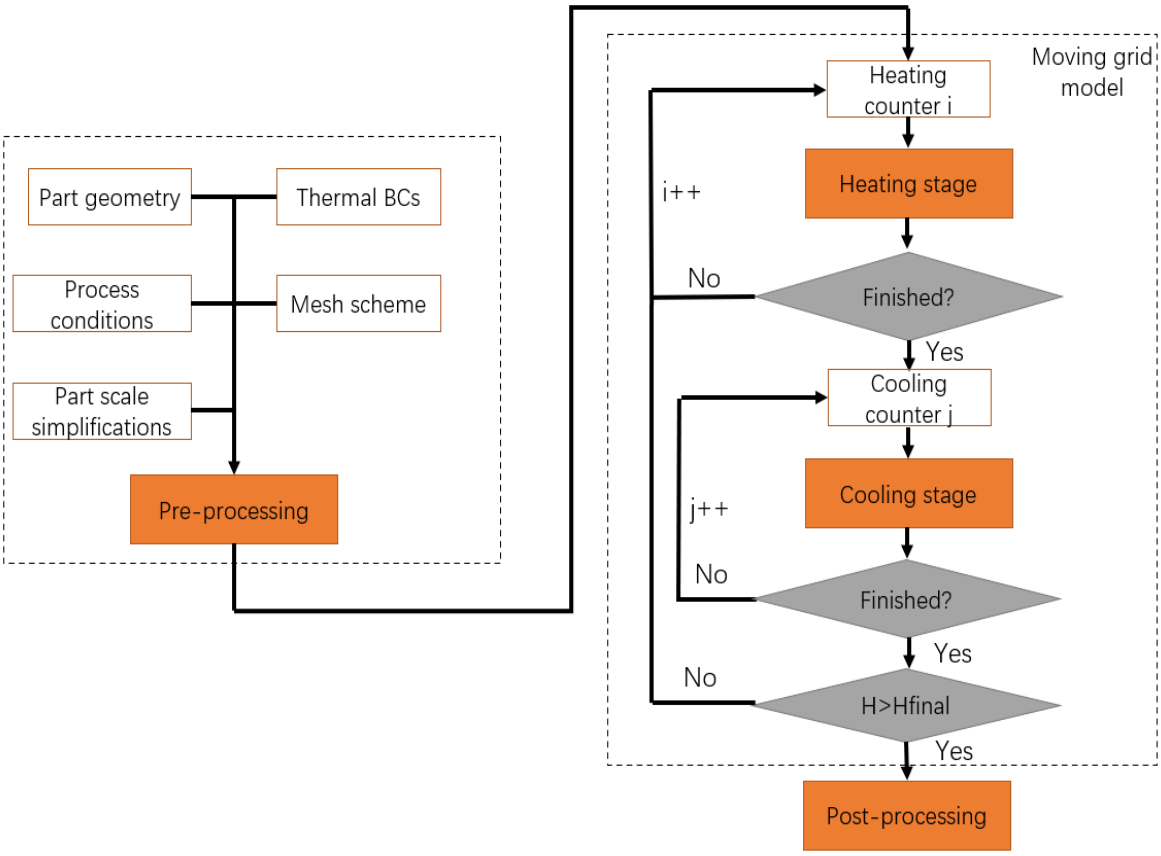

Figure 3-10: The flow chart for thermal field modelling.

piece. The expression is Eq. (3-20):

$$\bar{\theta} = \frac{\int \theta d\Omega}{\int d\Omega}, \tag{3-20}$$

where $\bar{\theta}$ is the average temperature value for the current time step and $d\Omega$ indicates the integral over the whole solid domain. In a structured mesh, Eq. (3-20) is calculated by summing up the average temperature for each element and then divided by the total area of solid domain.

In the next section, firstly a straightforward simulation for rectangular work piece is implemented. After that, a series of simulations are carried out with different combinations of process conditions and parameters. The temperature data are recorded and depicted with plots. In the end there is a thorough discussion focusing on how these factors affect the thermal distribution in the SLM process.

3-5-1 Rectangular work piece

In this section, the parameter value for $\dot{H}$ and Bi are 0.001 and 1.850×10^{-3} respectively. γ is 90° and heating/cooling time ratio λ is 1. In Fig. 3-11, the temperature field of a heating-cooling cycle during the deposition of layer 300 is presented. Fig. 3-11 (a), Fig. 3-11 (c) and Fig. 3-11 (e) are the temperature fields plotted in $x-\zeta$ space and Fig. 3-11 (b), Fig. 3-11 (d)

and Fig. 3-11 (f) are shown in $x-y$ space. Both the work piece and the base plate part are included in the contour plot.

Fig. 3-11 (a) and (b) display the heating stage when printing layer 300. The heat energy is supplied into the work piece from the laser source on the top part, which is modelled by the Dirichlet boundary condition, $\theta = 1$, the highest temperature appears at the top surface accordingly. Fig. 3-11 (c) to Fig. 3-11 (f) present the cooling stage, during which the laser source is temporarily turned off and a new layer of powder will be recoated. The heat thus dissipates from both the top surface and the bottom surface and it can be observed that nodal temperature drops very fast in the work piece. In Fig. 3-11 (g) and (h) a new layer is being built and the temperature on top rises again. This heating-cooling cycle is repeated during the simulation until the whole work piece is completely built.

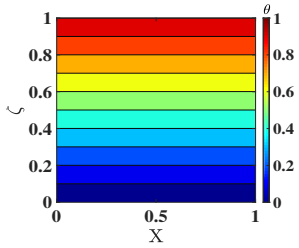

(a) manufacturing layer 300, heating, $X-\zeta$ space

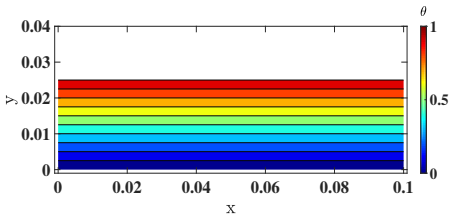

(b) manufacturing layer 300, heating, $x-y$ space

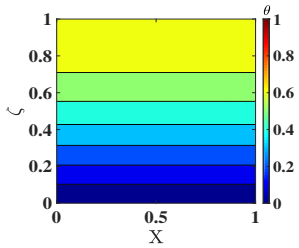

(c) manufacturing layer 300, cooling, $X-\zeta$ space

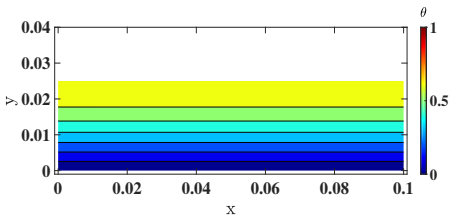

(d) manufacturing layer 300, cooling, $x-y$ space

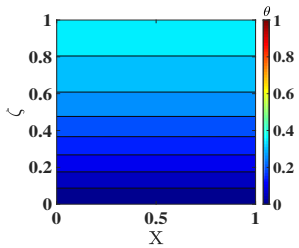

(e) manufacturing layer 300, cooling, $X-\zeta$ space

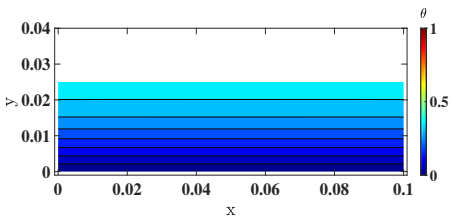

(f) manufacturing layer 300, cooling, $x-y$ space

Figure 3-11

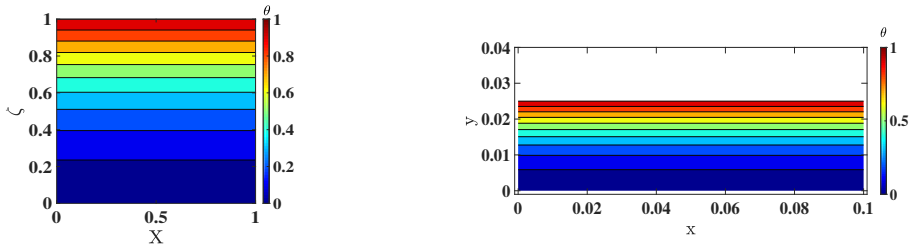

(g) manufacturing layer 301, heating, $x-y$ space (h) manufacturing layer 301, heating, $x-y$ space

Figure 3-11: A complete heating-cooling work cycle in SLM process. Both work piece and base plate are included in the plot. The $\dot{H}$ and Bi value is set to be 0.001 and 1.850×10^{-3}. Heating/cooling ratio λ is 1. All the temperature profiles are given in both $x-y$ space and $X-\zeta$ space. (a) and (b) is the temperature fields for the heating stage hence the top layer is kept at melting temperature. From (c) to (f) is the cooling stage, during which the heat losses from both top and bottom. Temperature in (g) and (h) is arising means a new layer is being built and the work piece is reheated again.

Under the same conditions and parameters, the sampled average temperature profiles are shown in Fig. 3-12 and the sampling time is 5 heating/cooling cycles for each case.

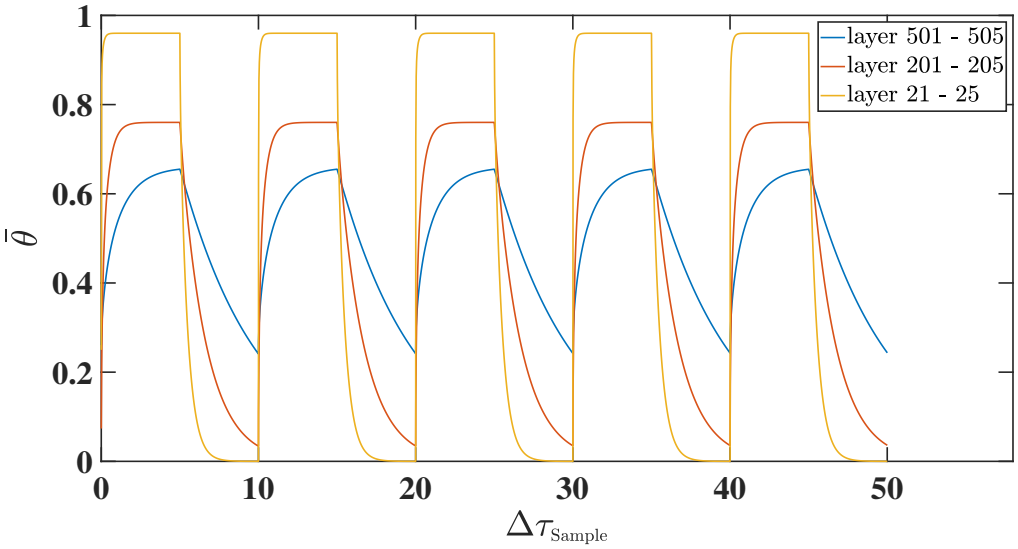

Figure 3-12: 5 heating-cooling cycles are sampled from the average temperature curves for rectangular work piece in different stages. Blue curve is the profile for layer 501 to layer 505, red curve is for layer 201 to layer 205 and orange curve is for layer 21 to layer 25.

Plotting the average temperature for all 600 layers in one figure is sometimes confusing and it is hard to get some detail information from it as too many data points are included. A clearer way to demonstrate the result is to sample the average temperature profile for several heating/cooling cycles for comparison purpose. In Fig. 3-12 this sampling time is 5 heating-cooling cycles and the x axis indicates the sampling time.

The orange curve in Fig. 3-12 indicates average temperature evolution from layer 20 to layer

25. It can be observed that during the heating stage, the average temperature increases to the peak temperature rapidly and keeps stable at that value until the cooling stage begins. In the cooling stage, the average temperature drops almost back to room temperature in a short amount of time and the average temperature stays around $\theta = 0$ until the next heating-cooling cycle. The temperature field in the rectangular work piece is a one dimensional distribution since thermal gradient does not exist in the horizontal direction.

It is important to note that with the number of layers built increases, the average temperature range in a work cycle is no longer that drastic due to the growing thickness of the work piece during the SLM process. In the early stage, the work piece is formed by only a few layers of material, heat is thus easily transferred within the small solid domain. Similarly, the procedure for heat loss is also remarkably fast because only a small amount of energy is stored in the solid work piece. As the work piece grows thicker and thicker, it is more difficult to quickly heat up or cool down the whole work piece . In addition, since the work piece shape in this simulation is just a rectangle, the top cross sectional area will not change during printing, which indicates the $\dot{H}$ value is constant. That explains the reason why in all three curves the heating-cooling cycle durations are the same.

3-5-2 Effect of the trapezoid inclination

A change in work piece geometry is well-known as a major factor that alters the local temperature distribution. The inclination γ is the parameter that controls work piece shape. In this group of simulation $\dot{H}$ is 0.001, Bi is 1.850×10^{-3} and heating-cooling ratio λ is 1. Selected values of γ tabulated in Table 3-2 are considered.

The temperature evolution for $\gamma = 45°$ and $\gamma = -45°$ are presented in Fig. 3-13 and Fig. 3-14 respectively.

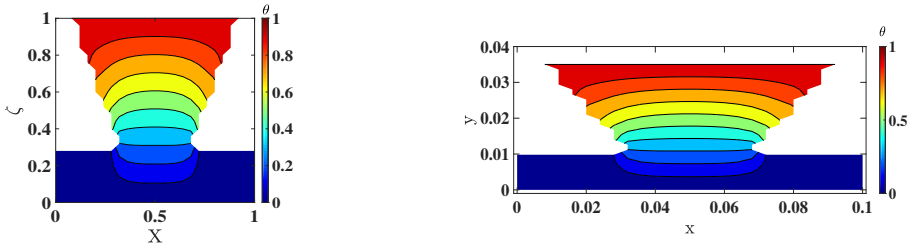

(a) manufacturing layer 500, heating, $X - \zeta$ space (b) manufacturing layer 500, heating, $x - y$ space

Figure 3-13

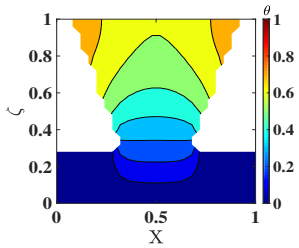

(c) manufacturing layer 500, cooling, $X-\zeta$ space

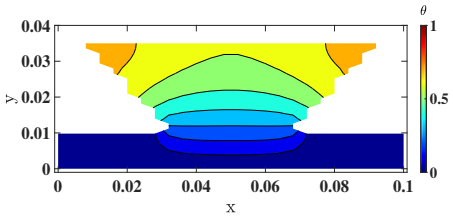

(d) manufacturing layer 500, cooling, $x-y$ space

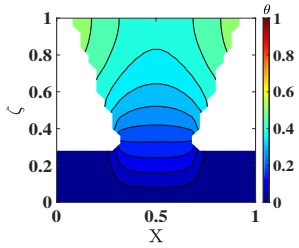

(e) manufacturing layer 500, cooling, $X-\zeta$ space

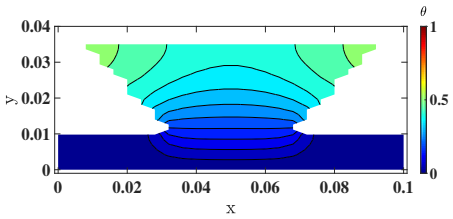

(f) manufacturing layer 500, cooling, $x-y$ space

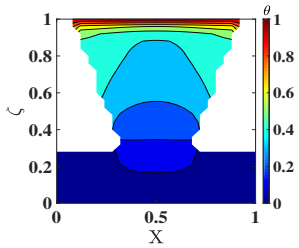

(g) manufacturing layer 501, heating, $x-\zeta$ space

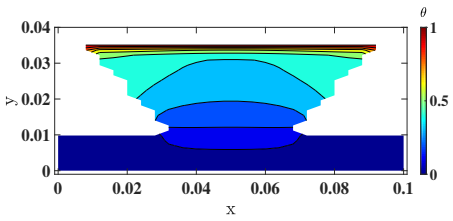

(h) manufacturing layer 501, heating, $x-y$ space

Figure 3-13: The heating-cooling cycle for $45°$ trapezoid. The domain of temperature plot contains both work piece and base plate. $\dot{H}$ and Bi value is set to be 0.001 and 1.850×10^{-3} and cooling ratio λ is 1. All the temperature profiles are given in both $x-y$ space and $X-\zeta$ space. (a) and (b) is the temperature profile of heating stage for manufacturing layer 500. (c) to (f) is the cooling stage in the same work cycle. (g) to (h) is the heating stage of a new work cycle for printing layer 501.

Fig. 3-13 depicts the temperature history printing layer 500 to layer 501. Temperature field in Fig. 3-13 follows the pattern as observed for the rectangular geometry: during the heating stage high temperature value appears on the top and low temperature value shows up at the bottom. In the cooling stage, the temperature level in all layers drops down. However, there is a significant difference concerning the shape of isotherms in the plot. The isotherms in $45°$ case are curves rather than parallel lines shown in the rectangular case and that suggests thermal gradient exists in the horizontal direction. The horizontal thermal gradient is caused by the staircase solid-powder interface depicted in Fig. 3-4. Recall that the heat boundary conditions for those jagged lines are insulated, demonstrating that no heat exchange with powder domain. Therefore, to some extent the heat transfer to the underlying layers is hindered and it seems the heat is 'stuck' in the small region near the lateral boundaries.

As for the nodes close to the midline of the trapezoid work piece, the heat transfer is not obstructed by the adiabatic boundaries, which leads to the phenomenon that the temperature near lateral boundaries are higher during both the heating and cooling stage.

Fig. 3-14 shows another example with a negative inclination. The temperature domain also includes both work piece part and the base plate. The rest process conditions and parameters are unchanged.

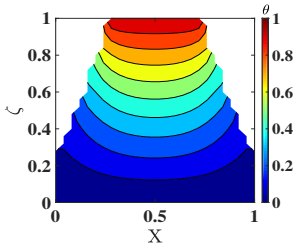

(a) manufacturing layer 500, heating, $X-\zeta$ space

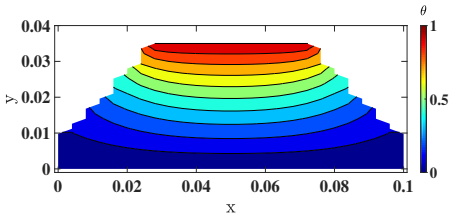

(b) manufacturing layer 500, heating, $x-y$ space

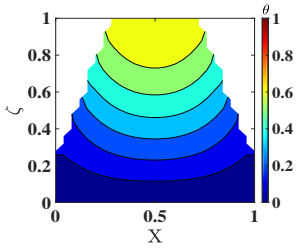

(c) manufacturing layer 500, cooling, $X-\zeta$ space

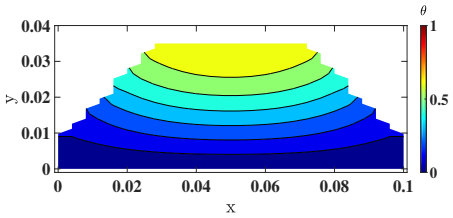

(d) manufacturing layer 500, cooling, $x-y$ space

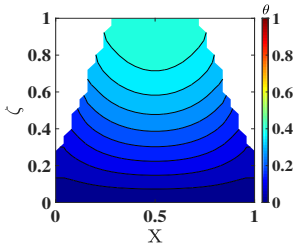

(e) manufacturing layer 500, recoating, $X-\zeta$ space

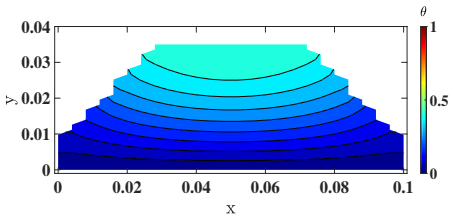

(f) manufacturing layer 500, recoating, $x-y$ space

Figure 3-14

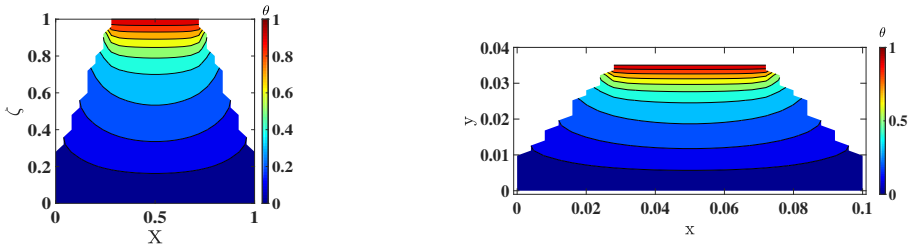

(g) manufacturing layer 501, reheating, $X-\zeta$ space (h) manufacturing layer 501, reheating, $x-y$ space

Figure 3-14: The heating-cooling heating-cooling cycle for $-45°$ trapezoid. The domain of temperature plot contains both work piece and base plate. $\dot{H}$ and Bi value is set to be 0.001 and 1.850×10^{-3} and cooling ratio λ is 1. All the temperature profiles are given in both $x-y$ space and $X-\zeta$ space. (a) and (b) is the temperature profile of heating stage for manufacturing layer 500. (c) to (f) is the cooling stage in the same work cycle. (g) to (h) is the heating stage of a new work cycle for printing layer 501.

The thermal gradient in the horizontal direction can be also noticed in Fig. 3-14 and the isotherms are bending to the direction of the bottom layer. The temperature near lateral boundaries is lower than that in the center since the stair shaped adiabatic boundaries make it difficult for heat to directly conduct to these corners from the top surface. However, it is much easier to cool down the boundary regions from the bottom. Furthermore, it can be concluded from both Fig. 3-13 and Fig. 3-14 that the side with longer width in work piece will dominate the heat transfer issues in a heating-cooling cycle.

The average temperature curves for different γ are depicted in Fig. 3-15.

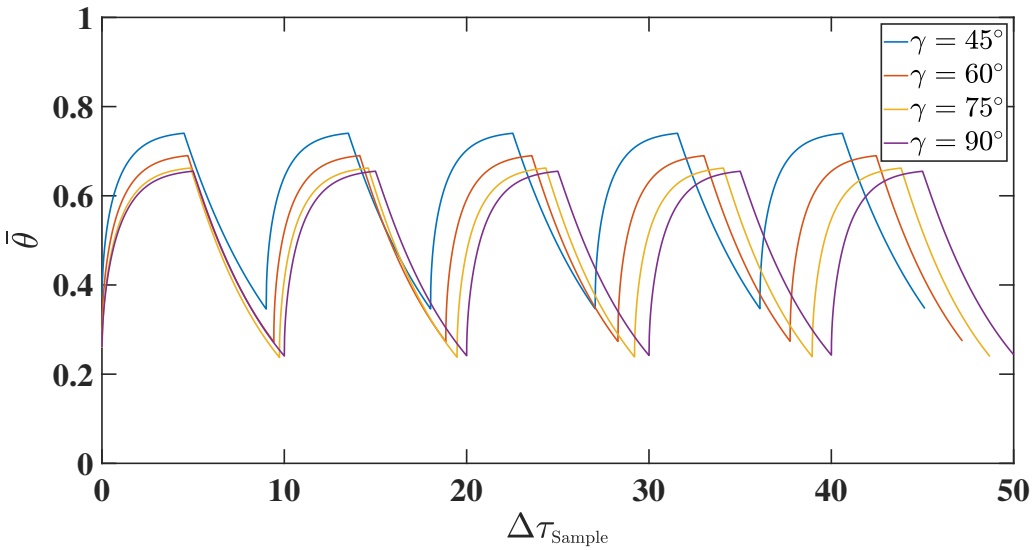

(a) Sampled average temperature curve for positive γ from layer 501 to 505

Figure 3-15

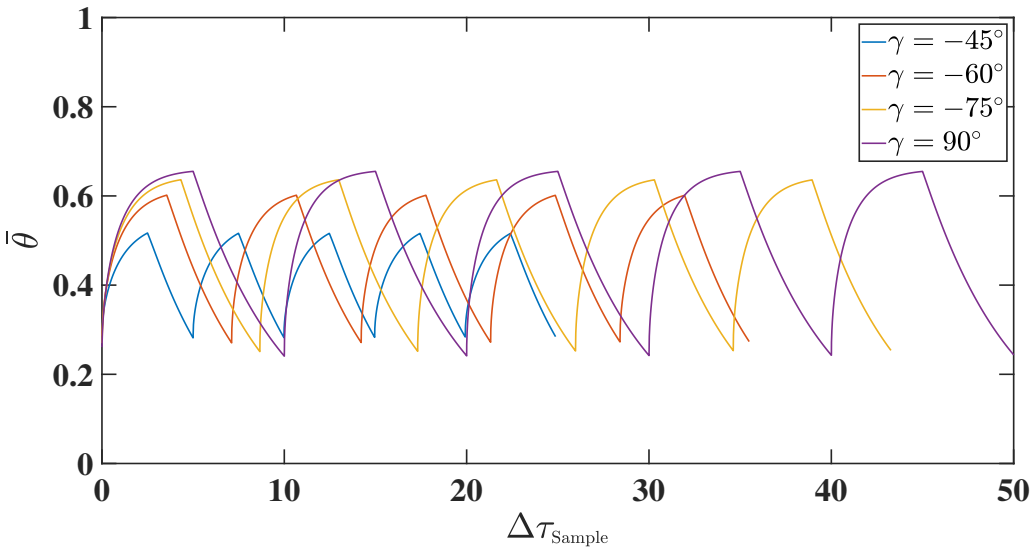

(b) Sampled average temperature curve for negative γ from layer 501 to 505

Figure 3-15: Sampled average temperature for different inclinations in the trapezoid work piece. $\dot{H}$ and Bi values are set to be 0.001 and 1.850×10^{-3} and cooling ratio λ is 1.

The sampling time for all the curves in Fig. 3-15 (a) and Fig. 3-15 (b) is 5 heating-cooling cycles and because of the different inclinations in the trapezoid work pieces, the duration of 5 heating-cooling cycles is not identical for each curve. These curves are put together for a better comparison.

In Fig. 3-15 (a), average temperature sample of the rectangular work piece is plotted together with temperature samples of the trapezoid with positive inclinations. Fig. 3-15 (b) shows the average temperature sample of the rectangular case with samples of trapezoid with negative inclinations. Recall that in Fig. 3-9 $\dot{H}$ changes in time for the trapezoid work piece, since the thickness for each layer is fixed, there is an inversely proportional relation between $\dot{H}$ and heating-cooling cycle duration. Consequently, the cycle duration difference is not evident for positive inclinations as these $\dot{H}$ values are very close to each other when approaching to the end of the simulation, which can be seen in Fig. 3-9. Oppositely, there is an obvious gap in cycle duration shown in Fig. 3-15 (b) because a large variance occurs in $\dot{H}$ value for negative inclinations.

Furthermore, work piece with positive inclination has a larger top surface and smaller bottom surface. Recalling that the Dirichlet boundary condition $\theta = 1$ is applied on the top and work piece bottom surface connects to low temperature base plate, hence a larger top surface suggests more energy input and a smaller work piece bottom surface implies less energy dissipation. Similarly, wide bottom surface leads to extra heat loss and narrow top surface limits the energy absorption. It can be seen from both Fig. 3-15 (a) and Fig. 3-15 (b) that by comparing with the temperature of $\gamma = 90°$, work pieces with positive inclinations tend to have higher average temperature level than work pieces with negative inclinations. This part geometry influence can be more apparently seen from Fig. 3-16.

Fig. 3-16 sketches the peak temperature value in the last layer of the simulation. It is observed that from $\gamma = 45°$ to $\gamma = 75°$, the peak temperature drops because the work piece

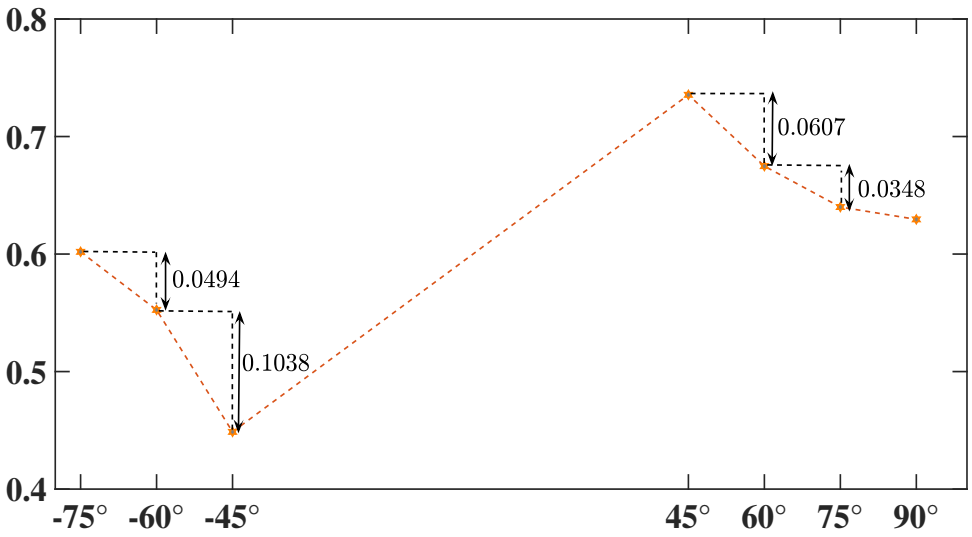

Figure 3-16: Peak temperature value in the last (600) layer with different γ values. By changing same amount of γ, the variation in temperature is lager among work pieces with negative inclinations since the top surface directly relates to the total energy absorption.

bottom surface area is decreasing, while from $\gamma = -45°$ to $\gamma = -75°$, the peak temperature is increasing since the top surface area expands in corresponding work piece geometry. In addition, by changing the same amount of inclination, peak temperature variation is larger in negative γ values, which denotes the influence of the top surface area is more pronounced on temperature field because it directly relates to energy input.

3-5-3 Cooling stage duration

The influence of the duration in the cooling stage is evaluated by λ which defines as the ratio between total heating time versus total cooling time in the whole process and therefore it can also represent heating duration versus cooling duration in each cycle. The parameter used in the simulation are $\dot{H} = 0.002$ and $Bi = 1.926 \times 10^{-3}$. The work piece inclination γ is 90°. Sampling time is 5 work cycle from layer 501. Value λ is switching between 6, 2 and 1. The temperature curve is shown in Fig. 3-17.

It is observed that the heating-cooling cycle duration in these 3 examples are different because smaller λ suggests longer cooling duration. Extended cooling time indicates work piece is exposed longer in the cooling protective gas, which not only lowers minimum average temperature value in a work cycle but reduces the peak temperature in every work cycle as well.

In conclusion, the effect of increasing λ implies a longer heating-cooling cycle and, at the same time, a lower level of work piece average temperature.

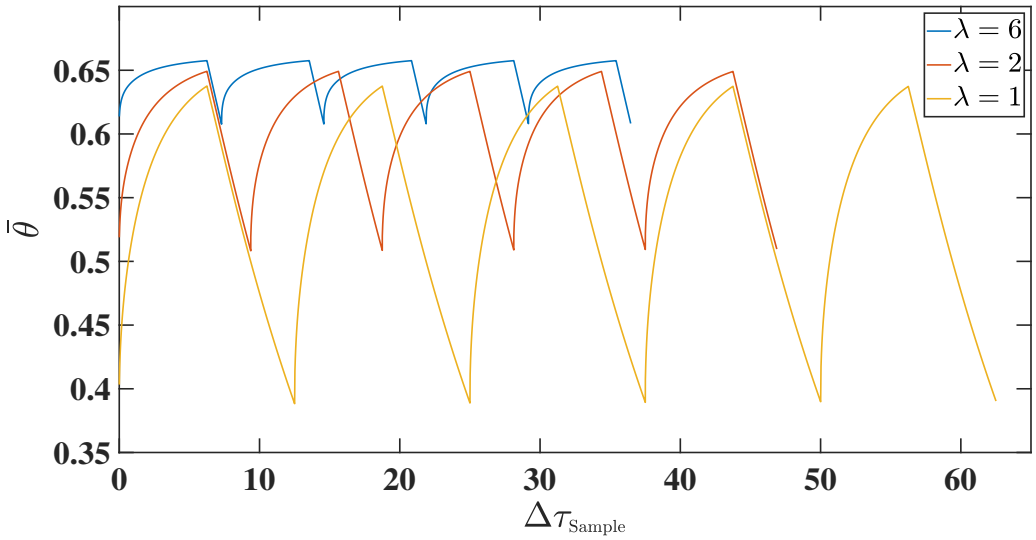

Figure 3-17: Sampled average temperature curve for different cooling time. Sampling time is 5 work cycle from layer 501 to layer 505. $\dot{H} = 0.002$, $Bi = 1.926 \times 10^{-3}$ and $\gamma = 90°$.

3-5-4 Dimensionless growth rate

Due to the connection between dimensionless grow rate $\dot{H}$ and Biot number Bi, the $\dot{H}$ values applied in the simulation are 0.0008, 0.001 and 0.002, the corresponding Bi values are 1.454×10^{-3}, 1.850×10^{-3} and 1.926×10^{-3}. γ value is $-45°$. 5 heating-cooling cycles are sampled from the average temperature profile. The simulation results are shown in Fig. 3-18.

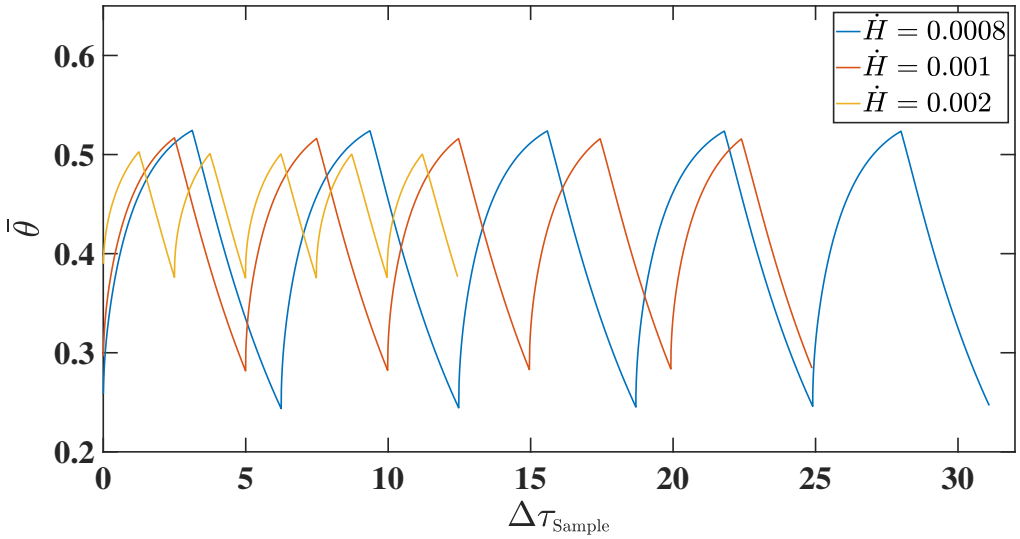

Figure 3-18: Sampled average temperature curve for different $\dot{H}$ value. Sampling time is 5 work cycle from layer 501 to layer 505. γ is a fixed value at $-45°$. When $\dot{H}$ increases from 0.0008, 0.001 to 0.002, Bi changes from 1.454×10^{-3}, 1.850×10^{-3} to 1.926×10^{-3}.

From the results derived in Section 3-2, the specific $\dot{H}$ value is calculated by $\dot{H} = \dot{l}l_0/\alpha$. Since printing speed $\dot{l}$ shows up in the numerator and thermal diffusivity α appears at the denominator in the expression of $\dot{H}$. Therefore, increasing the printing speed helps the work piece to grow faster in the simulation and decreasing the thermal diffusivity suggests heat transfer is more difficult to conduct in solid domain. The joint contribution of these two factors for $\dot{H}$ is thus presented in Fig. 3-18. It is depicted that a lager $\dot{H}$ will lead to shorter heating-cooling cycle duration and a larger gap between the peak value and the bottom value in average temperature curve while a smaller $\dot{H}$ is along with longer processing cycle duration and a small variation between the peak value and the bottom value in average temperature curve. Also, the highest peak temperature and lowest bottom temperature here both appear in curve with the $\dot{H} = 0.0008$.

3-5-5 Biot number

In this section, different Biot number values taken from Table 3-2 are applied in the simulation. The other parameters used are $\dot{H} = 0.0008$ and $\gamma = 60°$. Heating/cooling time ratio λ is 1 and sampling time is again 5 processing cycles from layer 501. The results are depicted in Fig. 3-19.

In Fig. 3-19 (a), all 3 curves in the plot almost overlap each other, the only part that some difference can be found is at the end of each cooling stage (for example the red circle region). The reason for such phenomenon is the effect of natural convection mainly depends on temperature difference at the beginning of the cooling stage. Hence the influence of increasing convection coefficient vanishes due to the considerable gap between melting temperature and protective gas temperature in the build chamber. Only when this temperature gap gradually narrows down then it can be seen from the Fig. 3-19 (a) that the temperature curve with a larger convection coefficient drops faster.

Fig. 3-19 (b) presents the magnification of the red circle region. Although the temperature difference can be noticed now, the influence of adjusting convection coefficient is still negligible.

3-5-6 Computational cost and accuracy

All the results that are collected by employing the moving grid method. It remains to compare the accuracy and the computational costs of the moving grid method in comparison to the element activation method reported in the literature.

With this purpose, a set of simulations are carried out with both moving grid method and element activation method under the same thermal boundary conditions. The process parameters for both methods are $\dot{H} = 0.001$, Bi is 1.850×10^{-3} and heating/cooling time ratio $\lambda = 1$. Selected values of γ ranging between $-75°$ - $90°$ will be considered. The total CPU time is measured in Fig. 3-20 as a function of γ. For accuracy comparison, the relative error for peak temperature value in the last layer are calculated as a function of γ, and the results from element activation method are used as a reference. These results are in Fig. 3-21.

From Fig. 3-20 a comprehensive improvement in computational time can be noticed. Compared with the moving grid method, during the element activation simulation, the total DOFs contained in the model is increasing in time, which gradually slows down the computation.

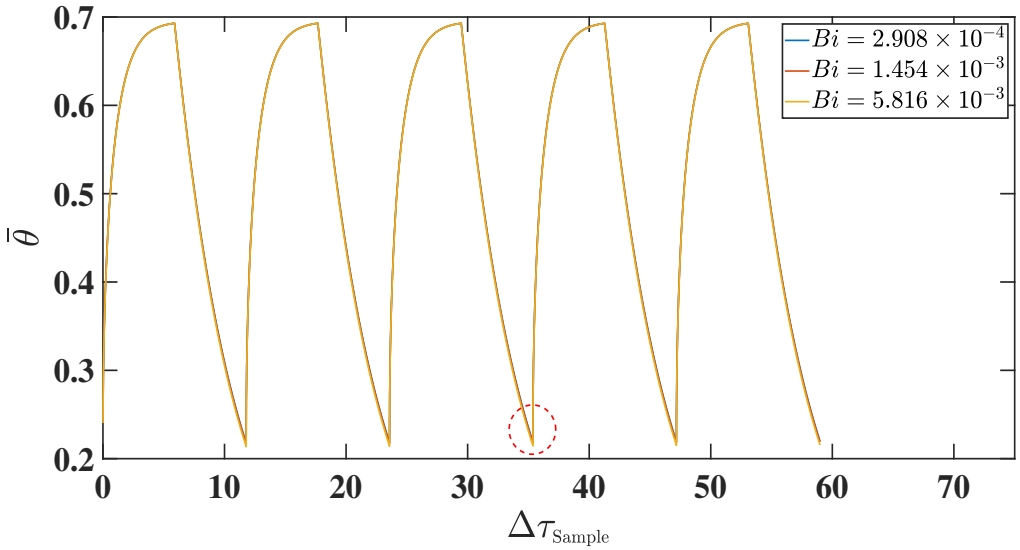

(a) Sampled average temperature for different Biot number

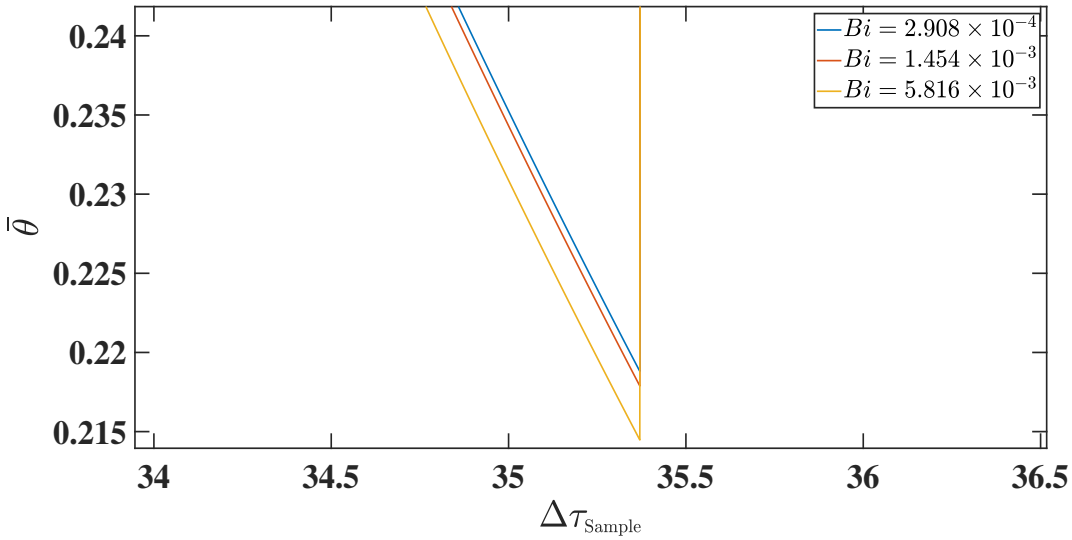

(b) Magnification of red circle region in figure (a)

Figure 3-19: Sampled average temperature curve for different Biot number. Sampling time is 5 work cycle from layer 501 to layer 505. γ is a fixed value at $60°$ for all 3 cases and $\lambda = 1$. $\dot{H}$ is chosen as 0.0008. Bi values used in simulation are 2.908×10^{-4}, 1.454×10^{-3} and 5.816×10^{-3}. (a) shows the effect of Biot number adjustment on temperature field and (b) is the red circle region in (a) after magnification.

This improvement in computational efficiency is even more pronounced when dealing with a trapezoid work piece because all the nodes will be traversed in every time step to check whether it belongs to solid domain or powder domain, which further brings burden to the simulation that already slows down by a growing number of elements and nodes. The ac-

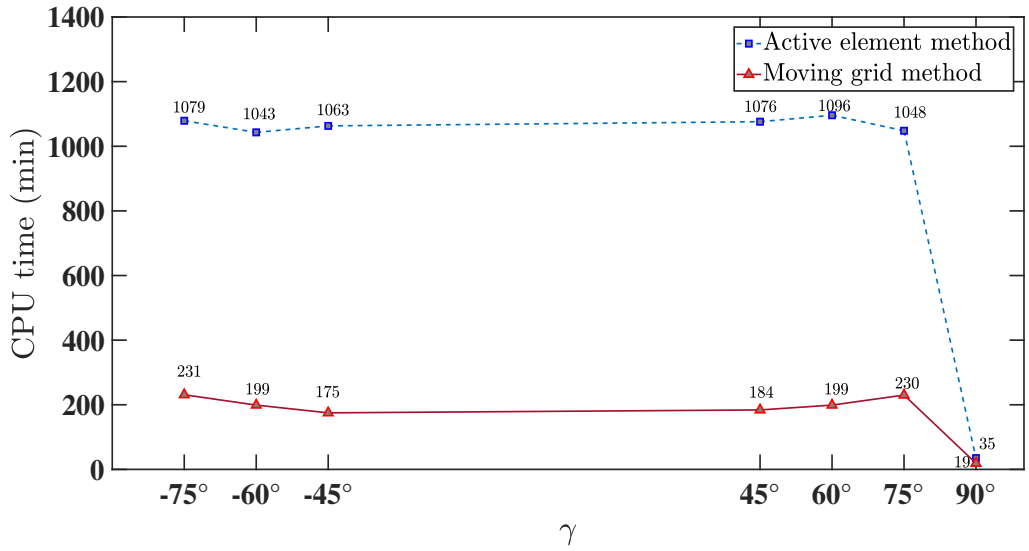

Figure 3-20: Computation time comparison between element activation method and moving grid method for various γ. Cluster setting are shown in Appendix II.

curacy of the moving grid method is evaluated by computing the relative error of the peak temperature value between these two methods when the process is finished. From the results

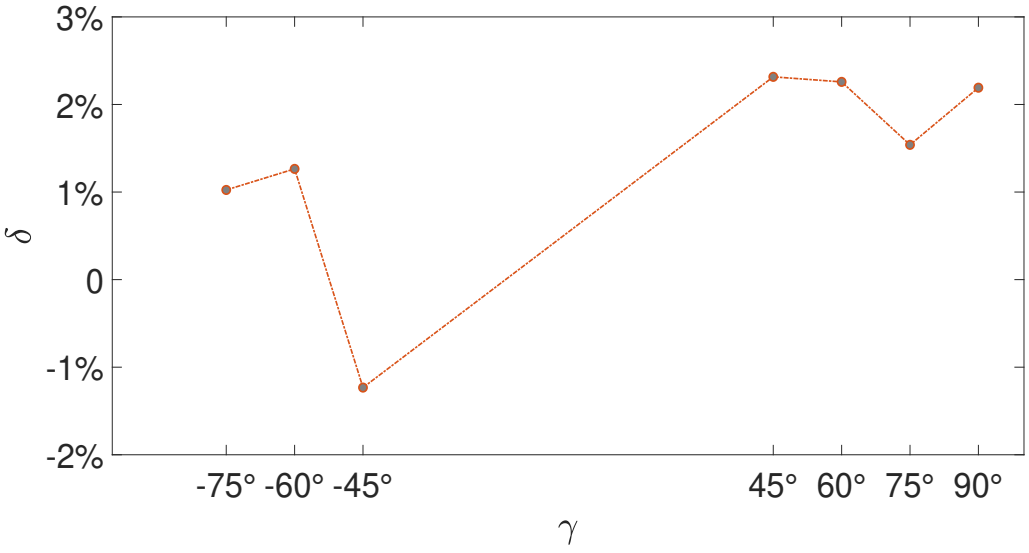

Figure 3-21: Calculated temperature difference between element activation method and moving grid element method. The temperature difference is calculated by subtract the peak temperature for moving grid method from the peak temperature value of element activation method in the last layer of the simulation process.

shown in Fig. 3-21, this level of error can be regarded as accurate enough when doing a fast estimation for the SLM process.

Moreover, by comparing with the results from other scientists who set up an experiment

framework, it is found that the average temperature values predicted by moving grid model are higher than experiment values and the nodal temperature in practice should be almost back to room temperature [36]. That is because in our model, it is assumed the heat load to be applied on a whole layer simultaneously, but in realistic manufacturing, the laser will move like as a point. As a consequence, For a single material point, it will only under heating at the moment the laser source just passes above it and after the laser source moves away, the material at that point cools down and re-solidified. Therefore, our assumption leads to more heat energy absorption into the work piece during the simulation and for a single material point, it endures much longer heating time than it should be.

Although with this defect, by referring the data from the moving grid model, the overall trend for temperature evolution can be reflected and the influence for various parameters are clearly displayed in our model.

3-6 Conclusions

In this chapter, a novel moving grid method is proposed based on a part-scale model to solve the thermal field in the SLM process. Simulations are carried out with a different set of process conditions and parameters and the corresponding results are shown and analyzed.

In Section 3-1, the idea of the moving grid is introduced with a 1D sample and then expand to a 2D domain. Governing equation based on the 2D domain is given and heat boundary conditions are defined over boundaries and interface and subsequently these equations are transferred into dimensionless form. Furthermore, the equations are discretized by an explicit finite difference scheme based on a square mesh. The allowable size of time step and spatial interval are also derived from the stability requirements. Besides, the idea of element activation method is briefly mentioned.

In Section 3-2, dimension parameters are determined and different part geometry in the simulation are represented by work piece inclination. In Section 3-3 three new dimensionless parameters are defined to integrate material properties and process conditions, which are dimensionless growth rate, Biot number and heating/cooling duration ratio.

In Section 3-5, simulations are carried out with a different set of dimensionless parameters and conclusions can be drawn from these simulation results. Work piece with positive inclination tends to result in higher average temperature while average temperature level is lower in those with negative inclination. The dimensionless growth rate has an impact on both heating-cooling cycle duration and the average temperature. A higher dimensionless growth rate will result in shorter heating-cooling cycle duration as well as smaller temperature fluctuation in one heating-cooling cycle. Increasing Biot number can help to reduce the average temperature in work piece but this effect is almost negligible. Smaller heating/-cooling time ratio indicates a longer duration of cooling, which will also lower the average temperature level in work piece. Eventually, the comparison between moving grid method and element activation method represents a remarkable improvement in computational cost and the accuracy is still maintained within an acceptable level.

Chapter 4

Thermal-mechanical coupling

In Chapter 3, a novel moving grid method is proposed to predict for temperature evolution during the SLM process. The simulations performed showed that an nonuniform temperature distribution is obtained in the work piece. Consequently, thermal expansion and contractions and the mechanical constraints such as the bonding between the base plate and work piece lead to the generation of part distortions and residual stresses. It is well-known that the root cause of residual stresses in the work piece is the existence of temperature gradients. To calculate the stress distribution, the temperature field data serve as the input for mechanical analysis and a finite element method is implemented. This thermal-mechanical analysis can be conducted considering either a strong-coupling or a weak coupling. With strong coupling, the temperature distribution will have an effect on the stress field and in turn, the distortions caused by thermal stress will also change the temperature field, which requires the thermal and mechanical analysis to be performed concurrently in each time step. The weak-coupling, or one-way coupling on the other hand, assumes thermal strains and stresses to be calculated on the basis of the temperature field. Therefore, thermal and mechanical analysis can be performed successively. For the sake of saving computational cost and given the fact that the effect of the stress and strains on the temperature field in this problem is negligible, the one-way coupling way is preferred in our simulation.

Also, according to the conclusion in Section 3-5, the work piece temperature in practice should be close to room temperature in the cooling stage. The temperature profile fed into thermal-mechanical coupling is thus modified as: temperature evolution during the heating stage is preserved as in Chapter 3, but the cooling stage is simplified by decreasing the temperature to room temperature in the entire domain. This modification also slightly reduces the computational time as now the cooling stage can be simulated in a single time step.

Furthermore, while predicting the residual stress, temperature dependent elastoplastic material behavior should be accounted for. However, here a temperature sensitive elastic material model is employed for simplicity to estimate thermal residual stresses [37].

Based on these assumptions, simulations are carried out with the moving grid method concerning work piece with different inclinations, readers can know from the results where the extreme stress and part distortions might occur. Besides, the simulations results for

element activation method under the same conditions are recorded as a reference. We will compare the computational efficiency between these two methods and the accuracy of the moving grid method are presented by computing the relative error.

4-1 Governing equations for thermal stress

The governing equation of stress analysis is defined on the same domain Ω as used in thermal analysis. With the elastic material model in place, the governing equation for this domain Ω can be expressed as:

$$\nabla \cdot \boldsymbol{\sigma} = 0, \tag{4-1}$$

where $\boldsymbol{\sigma}$ is the second order stress tensor.

$$\boldsymbol{\sigma} = \mathbf{C}\boldsymbol{\varepsilon}^{\mathrm{e}}, \tag{4-2}$$

The constitutive equation defines the stress-strain relation with a stiffness matrix $\mathbf{C}$, and $\boldsymbol{\varepsilon}^{e}$ is the second order elastic strain tensor. The total strain and thermal strain are prescribed as,

$$\boldsymbol{\varepsilon} = \boldsymbol{\varepsilon}^{\mathrm{e}} + \boldsymbol{\varepsilon}^{\mathrm{th}}, \tag{4-3}$$

$$\boldsymbol{\varepsilon}^{\mathrm{th}} = \alpha \Delta T \boldsymbol{I}, \tag{4-4}$$

where total strain $\boldsymbol{\varepsilon}$ contains elastic strain $\boldsymbol{\varepsilon}^{\mathrm{e}}$ and thermal strain $\boldsymbol{\varepsilon}^{\mathrm{th}}$. $\boldsymbol{I}$ is the identical tensor. α, ΔT denote thermal expansion coefficient and temperature difference respectively. Furthermore, considering the size of work piece we defined in Chapter 3: the work piece depth is $d_0 = 0.1$ m while the work piece thickness is only $l_0 = 0.01$ m at the beginning of the simulation, the depth is much larger than the thickness. The plane strain assumption is thus applied when calculating the stress and the expression of stress components in a single element written in Voigt notation as:

$$\begin{bmatrix} \sigma_{11} \\ \sigma_{22} \\ \sigma_{12} \end{bmatrix} = \frac{E\,(1-\nu)}{(1+\nu)\,(1-2\nu)} \begin{bmatrix} 1 & \frac{\nu}{1-\nu} & 0 \\ \frac{\nu}{1-\nu} & 1 & 0 \\ 0 & 0 & \frac{1-2\nu}{2(1-\nu)} \end{bmatrix} \begin{bmatrix} \varepsilon_{11} \\ \varepsilon_{22} \\ \gamma_{12} \end{bmatrix} - \frac{E\alpha\Delta T}{1-2\nu} \begin{bmatrix} 1 \\ 1 \\ 0 \end{bmatrix} \tag{4-5}$$

4-2 Mechanical boundary conditions

The boundary conditions we will use in mechanical analysis is depicted in Fig. 4-1 below.

From which it can be seen all the boundaries are free to deform except the bottom surface of the base plate, which is rigidly constrained. The corresponding mechanical boundary conditions can be written as:

$$\mathbf{u} = 0, \text{ on } \partial\Omega_{\mathrm{bot}}, \tag{4-6a}$$

$$\mathbf{t} = 0, \text{ on } \partial\Omega_{\mathrm{top}} \cup \partial\Omega_{\mathrm{lat}} \cup \partial\Omega_{\mathrm{int}}, \tag{4-6b}$$

where $\mathbf{u}$ indicates displacement and $\mathbf{t}$ is surface traction.

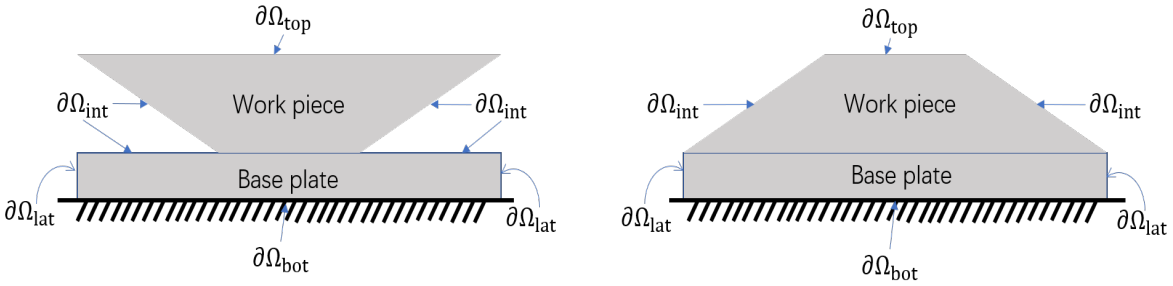

Figure 4-1: Work piece with positive inclination and negative inclination, both of the work pieces are constrained from the bottom side.

4-3 Temperature dependent material properties

During the SLM process, the temperature inside the build chamber varies between the room temperature and the metal point of the metal, which drastically influences the material properties. In particular, thermal expansion coefficient α, Young's modulus E and Poisson's ratio ν are the three key factors which may change the resulting stress prediction. Therefore, these three material properties will be accurately defined based on the local instantaneous temperature value. It need to notified that the material properties here are representative of Inconel 718 (bulk metal properties used).

The empirical formula to describe temperature dependent Young's modulus in the temperature range $200\text{K} < T < 1366\text{K}$ is :

$$E = 2.216171\times10^{11} + 1.071145\times T^8 + 118609.2T^2 - 77.87834T^3, \text{ (E in Pa, T in K) [38].} \quad (4\text{-}7)$$

and the curve is plotted in Fig. 4-2.

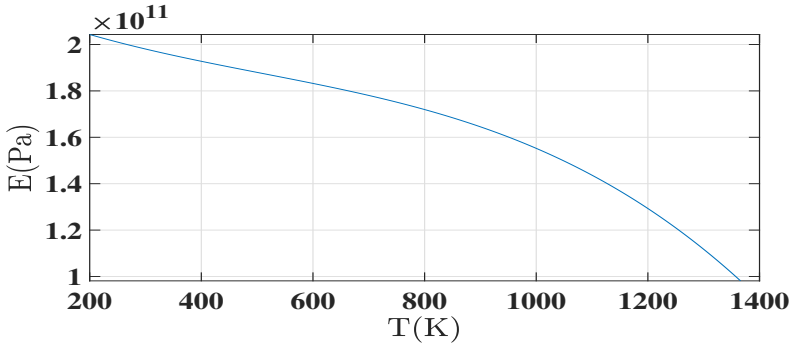

Figure 4-2: The temperature dependent Young's modulus value of Inconel 718.

For thermal expansion coefficient, the empirical model in temperature range $33\text{k} < T < 1144\text{K}$ is :

$$\alpha = 8.492399\times10^{-6} + 1.858772\times10^{-8}T - 2.145462\times10^{-11}T^2 + 7.596296\times10^{-15}T^3 + 2.254909\times10^{-18}T^4, \text{ (α in 1/K, T in K) [38].} \quad (4\text{-}8)$$

with the curve plotted in Fig. 4-3. Temperature dependent Poisson's ratio is a piecewise

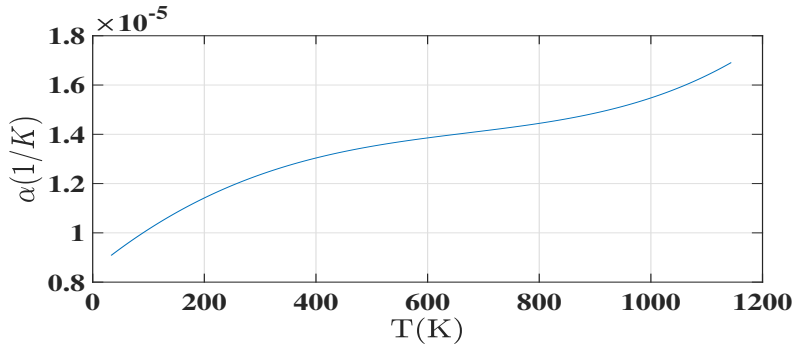

Figure 4-3: The temperature dependent thermal expansion coefficient value of Inconel 718.

function that in the temperature range of 200K $< T <$ 800K with the expression:

$$\nu = 0.3046558 - 9.703382 \times 10^{-5}T + 7.919159 \times 10^{-8}T^2, \text{ (ν is dimensionless and T in k) [38].} \tag{4-9}$$

and for temperature range in 800k $< T <$ 1366K the formula is:

$$\nu = -0.3168756 + 0.001877752T - 2.021026 \times 10^{-6}T^2 + 7.534566 \times 10^{-10}T^3 \text{ [38].} \tag{4-10}$$

The piecewise function is plotted in Fig. 4-4. It is worth noting that the upper bound of the

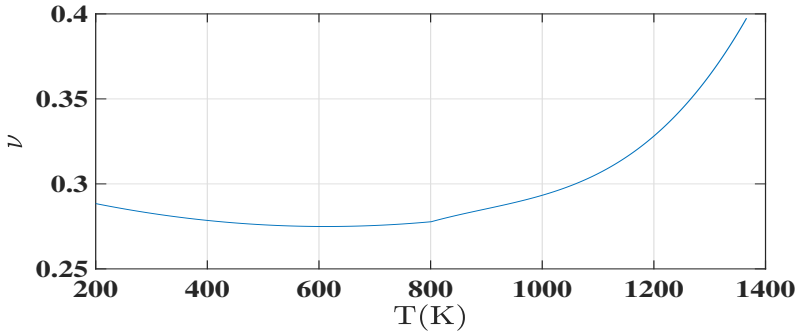

Figure 4-4: The temperature dependent Poisson's ratio value of Inconel 718.

empirical formula may not reach the metal melting temperature. The solution is to introduce the concept of 'cut-off temperature' [36]. The value of 'cut-off temperature' is defined as the upper limit in the empirical model and when node temperature goes above the cut off value, the material properties remain unchanged as the value used at cut off temperature.

4-4 Finite element analysis

It is known that in thermal analysis part a mesh with 625 square elements was used. Here in thermal mechanical analysis, each square element is further divided into 2 constant strain triangular elements for computational simplicity. Moreover, only one gauss point is defined within each triangular element so that the reduced integration scheme can be used. Each node in the triangular element has 2 DOFs.

The thermal mechanical analysis requires temperature field data as input and it is admitted from our assumption that the cooling stage is further simplified by resetting all nodal temperature to room temperature. The parameters used in the thermal analysis are dimensionless grow rate $\dot{H} = 0.001$, $Bi = 1.850 \times 10^{-3}$ and inclination γ see Table 3-2.

During the simulation, the thermal heating/cooling cycle is followed by a mechanical analysis to calculate the stress field. The stress calculation only captures the moment after the nodal temperature back to room temperature. The temperature difference is thus defined between the nodal temperature in the last time step of the previous heating stage and the room temperature. In the next heating stage, the work piece temperature field rise again after cooling down to room temperature . However, the stress analysis here is considered to be independent, which indicates the stress field obtained in the current layer will not rely on the stress history in previous layers. Besides, based on our assumption for the simplified model, it can be expected that the high stress value will occur in the work piece. It is assumed that all the calculations are confined in the elastic domain and the stress level will not exceed the yield strength.

4-5 Results and discussions

In this section, a stress simulation with a rectangular shape work piece is implemented first and the thermal stress mechanism is explained with the results. Simulations for different inclinations ranging from $\gamma = -75°$ to $\gamma = 90°$ are also conducted to show the possible influence of part geometry on stress distribution. The comparison results between the moving grid method and element activation method in computational efficiency and accuracy are shown at the end of the section. The computational efficiency is evaluated by CPU time. As for accuracy, since at the end of the simulation the stress data of the moving grid method and the element activation method are based on different mesh (the node number are different in the build direction), the data of moving grid method will be interpolated on the same mesh as used by element activation method. Then a root mean square error calculation is implemented to compare the accuracy. All the simulation results will be shown in $x-y$ space.

Following the definition for stress calculation described in Section 4-4, the stress field σ_{xx} and σ_{yy} for different layers can be computed and the results are plotted in Fig. 4-5 and Fig. 4-6 respectively.

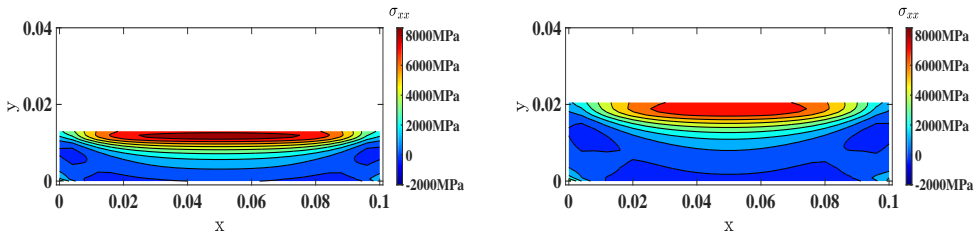

(a) σ_{xx} in layer 60

(b) σ_{xx} in layer 210

Figure 4-5

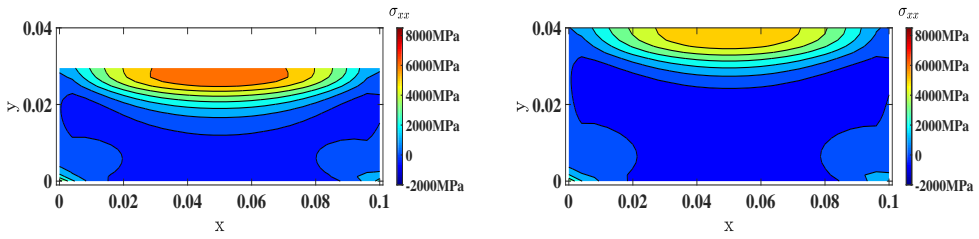

(c) σ_{xx} in layer 390 (d) σ_{xx} in layer 600

Figure 4-5: σ_{xx} for rectangular work piece in different layers

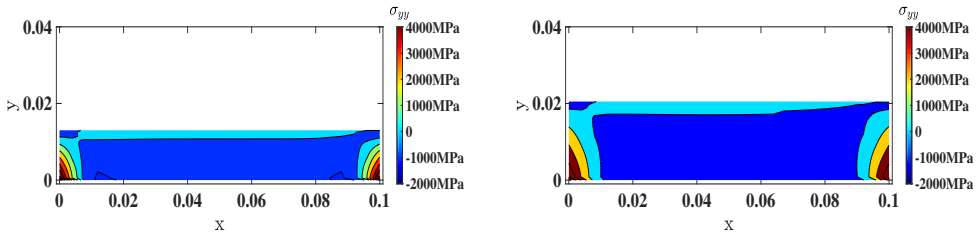

(a) σ_{yy} in layer 60 (b) σ_{yy} in layer 210

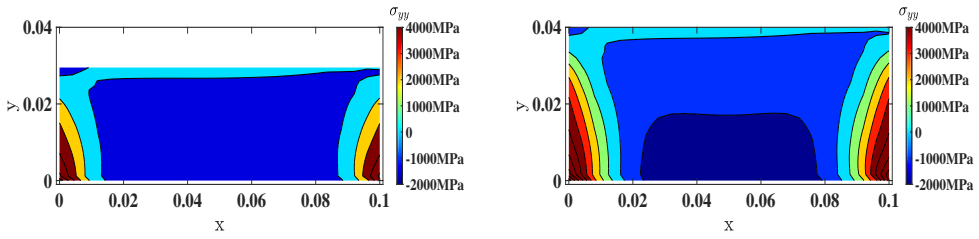

(c) σ_{yy} in layer 390 (d) σ_{yy} in layer 600

Figure 4-6: σ_{yy} for rectangular work piece in different layers

From the Fig. 4-5, it can be discovered that tensile stresses always appear at the top part of the work piece while the lower part is dominated by compressive stresses. Also, As the work piece grows in time, the tensile stresses on the top are gradually decreasing. The results in Fig. 4-6 represent that compressive stresses are noticed at central part in work piece and large tensile stresses occurs near the lateral boundary.

The causes for such kind of σ_{xx} distribution in work piece can be traced back to heating-cooling cycles in the SLM process. During the heating stage, several layers on the top will be heated and thus these layers are at a temperature far above the temperature of underlying layers. At this moment, the top most layers at elevated temperatures have the tendency to expand but this expansion is restricted by the underlying part whose temperature is much lower. Consequently, this expansion will lead to a contraction in the top part and tension in

the bottom part. After the heat source is temporarily removed, the temperature of the top layer will rapidly drop down because of the stark temperature contrast between the top most layer and the surrounding protective gas, during which the top part is under contraction. Because the temperature gradient exists, this contraction is not consistent: the layers on the top tend to contract more while the underlying layers contract less. Hence contraction in the top part will be constrained by lower part resulting in tensile stresses in the recently build layers and compressive stresses in the underlying layers. It can be concluded that the final stress state mainly develops from the thermal contraction in the cooling stage and the same type of stress distribution will show up time after time whenever a new layer is deposited.

The stress decreasing at topmost layers can be explained by the conclusion in Section 3-6: it becomes harder to heat up the whole work piece because work piece thickness is growing during the simulation and the corresponding average temperature level is thus reducing with time. When calculating the thermal stress, temperature difference is a dominant factor and it is computed as the subtraction between the room temperature and the instantaneous nodal temperature. The decrease in work piece average temperature level cuts down this temperature difference, which causes lower stress value on the top part.

The compressive stresses in σ_{yy} are caused by the contraction happens in the work piece during the cooling stage. Due to the temperature gradient in the work piece, the layers on the top tend to contract more than underlying layers, which results in lower layers are pressed by the top layers. The compressive stresses are hence induced in the central part. However, the contraction in the middle of the work piece also forces the material near the lateral boundary to stretch and this stretch is restricted by bottom constraint, generating the tensile stresses near lateral boundaries.

To summarize briefly, the stress state in work piece mainly caused by a sharp temperature gradient on the top part during the cooling stage as well as the bottom mechanical constraint. After knowing the mechanism of how thermal stresses are induced, a set of simulations are carried out on work piece with different inclinations. The stress field and distortion prediction after the part geometry is completely built are shown in Fig. 4-7 and Fig. 4-8.

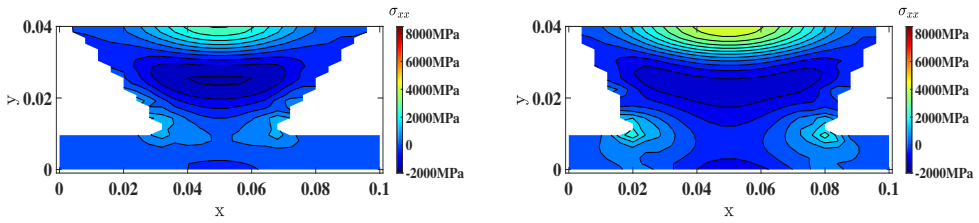

(a) σ_{xx} for $\gamma = 45°$ in final state

(b) σ_{xx} for $\gamma = 60°$ in final state

Figure 4-7

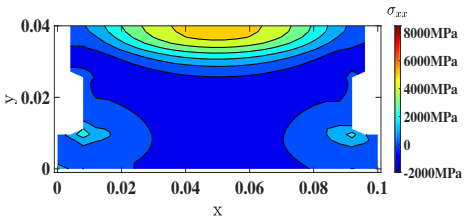

(c) σ_{xx} for $\gamma = 75°$ in final state

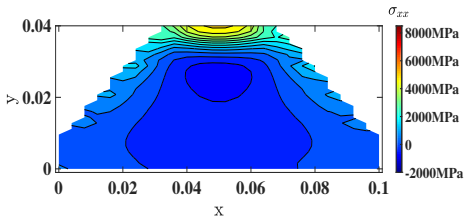

(d) σ_{xx} for $\gamma = -45°$ in final state

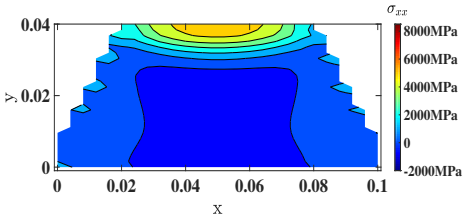

(e) σ_{xx} for $\gamma = -60°$ in final state

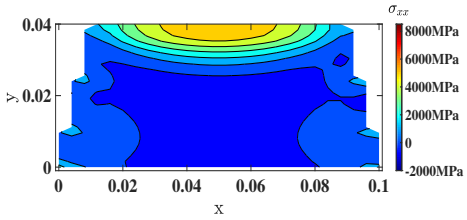

(f) σ_{xx} for $\gamma = -75°$ in final state

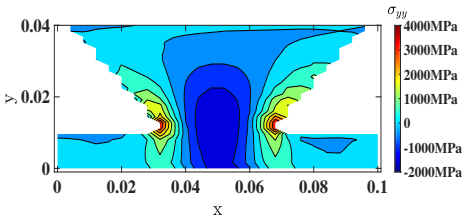

(g) σ_{yy} for $\gamma = 45°$ in final state

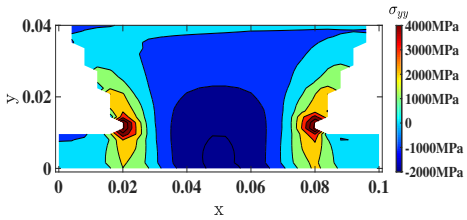

(h) σ_{yy} for $\gamma = 60°$ in final state

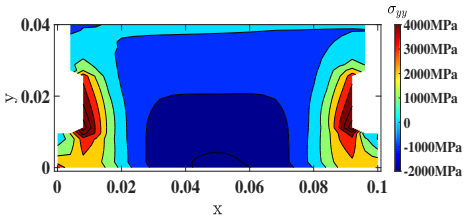

(i) σ_{yy} for $\gamma = 75°$ in final state

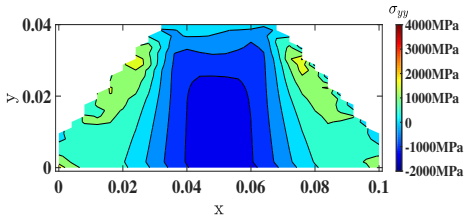

(j) σ_{yy} for $\gamma = -45°$ in final state

Figure 4-7

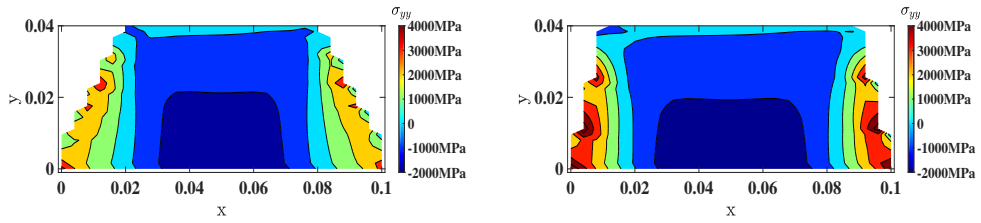

(k) σ_{yy} for $\gamma = -60°$ in final state

(l) σ_{yy} for $\gamma = -75°$ in final state

Figure 4-7: σ_{xx} and σ_{yy} for different inclinations after part geometry is completely built. x, y dimensions are scaled by meter.

Although in different inclinations, it can be seen from Fig. 4-7 that for σ_{xx}, tensile stresses always appear on top layers while compressive stresses dominate the lower layers. The reason for such distribution has been explained for rectangular case, due to the inconsistent thermal contraction in the cooling stage. For σ_{yy}, compressive stresses show up in the center of the work pieces because the top layers tend to shrink more than the underlying layers and hence press on these lower layers. Furthermore, the contraction in the central part also forces material near the lateral boundaries to expand. However, since the bottom base plate is clamped, tensile stresses are observed near the lateral boundaries and the bottom corner. An obvious stress concentration is seen on the interface between the base plate and the work piece in part geometry with positive inclination, which is caused by the sudden change in cross sectional area. There are also some local stress concentrations on lateral boundaries, but these concentrations are artificial and result from finite resolution of the structured grid.

The final distortions can be predicted base on stress distribution shown in Fig. 4-8.

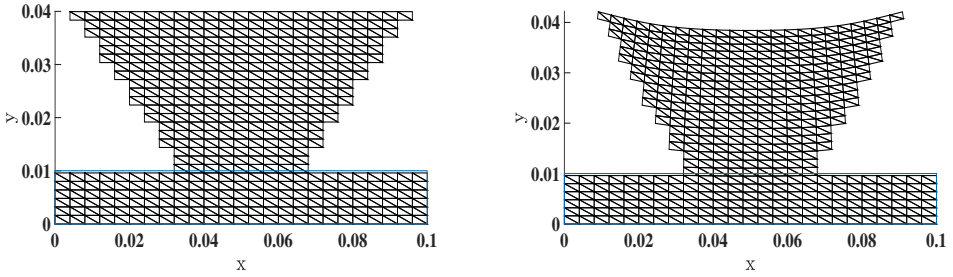

(a) Final part geometry without thermal distortion, $\gamma = 45°$

(b) Final part geometry with thermal distortion, $\gamma = 45°$

Figure 4-8

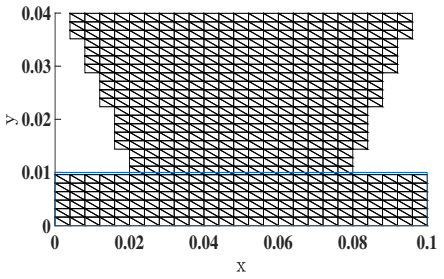

(c) Final part geometry without thermal distortion, $\gamma = 60^\circ$

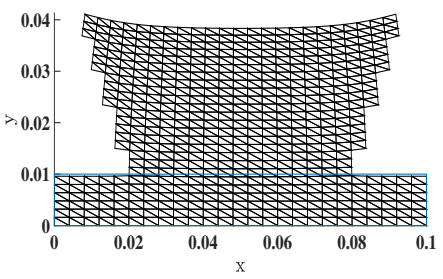

(d) Final part geometry with thermal distortion, $\gamma = 60^\circ$

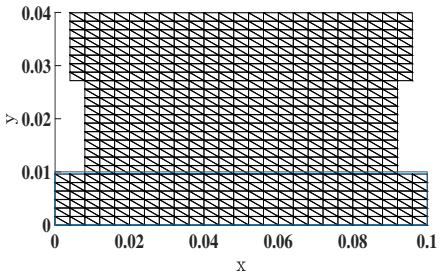

(e) Final part geometry without thermal distortion, $\gamma = 75^\circ$

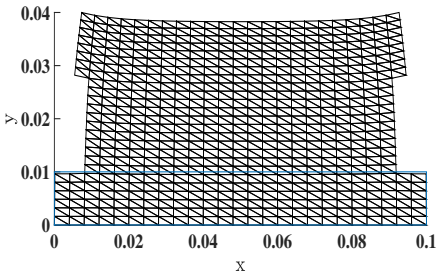

(f) Final part geometry with thermal distortion, $\gamma = 75^\circ$

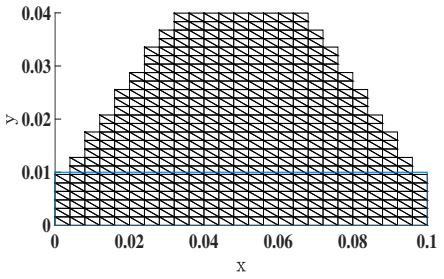

(g) Final part geometry without thermal distortion, $\gamma = -45^\circ$

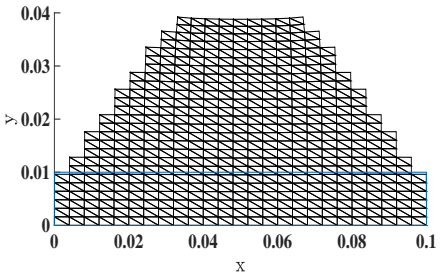

(h) Final part geometry with thermal distortion, $\gamma = -45^\circ$

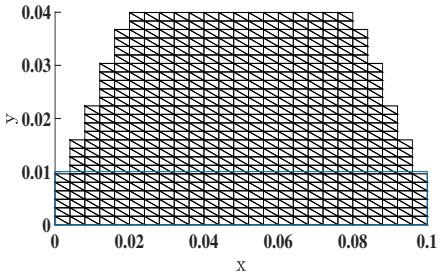

(i) Final part geometry without thermal distortion, $\gamma = -60^\circ$

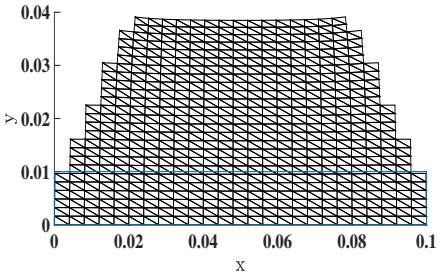

(j) Final part geometry with thermal distortion, $\gamma = -60^\circ$

Figure 4-8

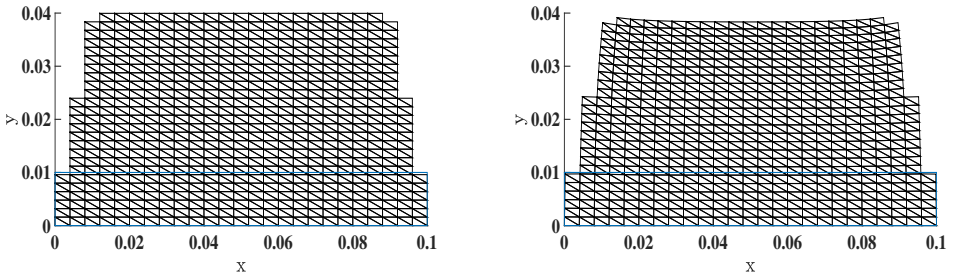

(k) Final part geometry without thermal distortion, $\gamma = -75°$

(l) Final part geometry with thermal distortion, $\gamma = -75°$

Figure 4-8: Comparison between part distortion and their original shape in trapezoid work piece with different inclinations. Part surrounded by blue rectangle is the base plate. x, y dimensions are scaled by meter

The distortions in part geometry are thermal shrinkage caused by the sudden temperature drop in the cooling stage. If the constraint is removed, the part geometry is expected to tilt up according to the internal residual stress distribution.

It is acknowledged that the thermal stress is influenced by both the temperature gradient in work piece and the constraints. In order to reduce the stress level, based on the conclusions in Section 3-6, a negative work piece inclination is recommended, which can be proved by results in Fig. 4-7 (d) and Fig. 4-7 (j). However, the σ_{xx} distribution in Fig. 4-7 (a) and Fig. 4-7 (b) display an opposite trend as we predicted. This is because the part geometry with positive inclination is much easier to deform under stress, which can be demonstrated by checking the distortion plots in Fig. 4-8 (b) and Fig. 4-8 (d). The residual stresses stored in the work piece are partly released by these distortions. Therefore, it is recommended to build the part geometry with negative inclinations during SLM process and try to avoid positive inclinations as a part geometry with an inclination is easy to deform under stress and may induce stress concentration.

Besides, according to Section 3-6, more measures can be proposed to reduce the stress level in work piece. For example, choosing a material with larger dimensionless growth rate $\dot{H}$, which would likely to give a lower average temperature. Another useful technique that already widely used in industry is to preheat the build chamber to a higher temperature before manufacturing so that the temperature gap during the cooling stage is smaller [37, 39, 40].

4-6 Computational cost and accuracy

It is expected that the moving grid scheme will improve the computational efficiency. Therefore, a set of simulations are run for both element activation method and moving grid method, during which all the process conditions and parameters are kept the same. Simplifications made in moving grid method are also held for the element activation method. The comparison results for time cost are plotted in Fig. 4-9.

From Fig. 4-9, it is quite obvious to notice that time consumption in the simulation is greatly reduced by using the moving grid approach as the increasing DOFs in element activation method will slow down the simulation. This improvement is more pronounced when building

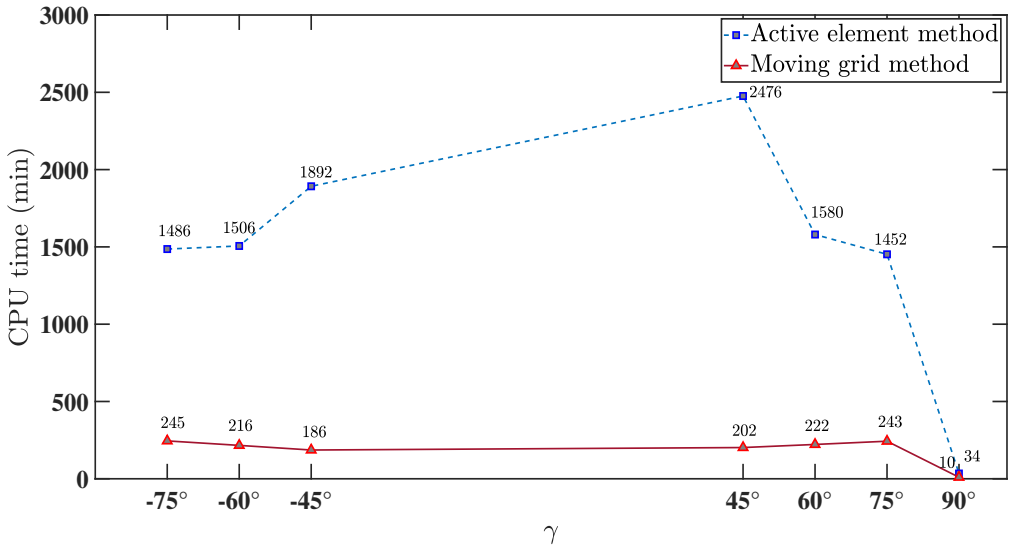

Figure 4-9: Time comparison for thermal-mechanical modelling between moving grid method and element activation method. Cluster settings are shown in Appendix II.

a part geometry with an inclination since more time is needed to monitor the nodal property in each time step.

The accuracy of the simulation results obtained by the moving grid method is evaluated by calculating the root mean square deviation for nodal stress quantities after the part geometry is completely built. Since the total node numbers are different for each of the methods at the end of the simulation, the stress field data of moving grid method are first interpolated on a grid that is identical to the grid used in element activation method and subsequently the root mean square deviation is calculated. The results are depicted in Fig. 4-10.

Fig. 4-10 suggests the root mean square deviation for σ_{xx} and σ_{yy} as a function of the inclination γ. An abnormal data point occurs when $\gamma = 75°$, the deviation suddenly increases at this point. In order to find the cause for this deviation, the σ_{yy} distributions at this point are plotted in Fig. 4-11.

By checking the σ_{yy} distribution from both the element activation method and moving grid method after the linear interpolation, it is found that a stress concentration occurs around the corner marked by the red circle in Fig. 4-11 and the predicted stress values are also divergent there. This stress concentration is artificial and induced by finite mesh resolution because a few nodes in the vicinity are judged as powder, which looks like a crack in Fig. 4-11 (a) and Fig. 4-11 (b). Besides, the linear interpolation itself can also bring uncertainties into the result. Despite the discrepancy in predicted stress value when $\gamma = 75°$, the overall trend for stress distribution is clearly reflected, and for the rest of the data points the deviations are acceptable.

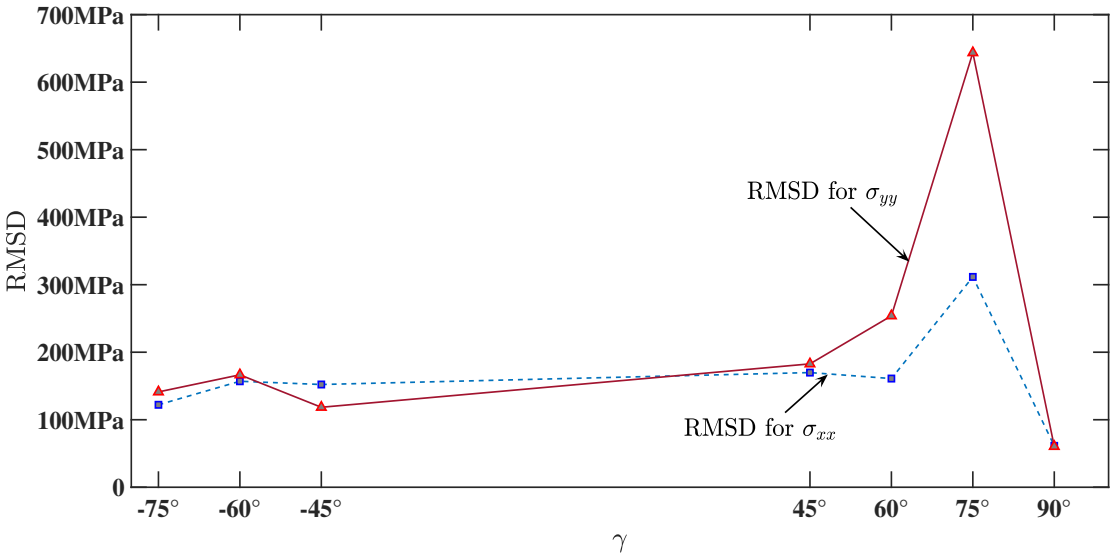

Figure 4-10: Root mean square deviation as a function of γ between the moving grid method after linear interpolation and the element activation method.

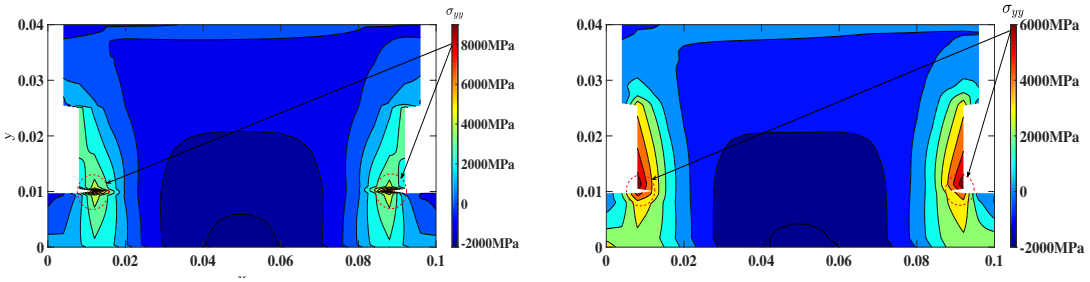

(a) σ_{yy} distribution when $\gamma = 75°$ predicted by the element activation method

(b) σ_{yy} distribution when $\gamma = 75°$ predicted by moving grid method after linear interpolation

Figure 4-11: σ_{yy} distribution data from both element activation method and interpolated moving grid method when $\gamma = 75°$.

4-7 Conclusions

In this chapter a thermal-mechanical model is defined with the following assumptions: (i) The work piece is purely elastic and it is assumed that the maximum stress will not exceed the yield strength; (ii) The cooling stage is simplified by resetting all the nodal temperature back to the room temperature, the heating stage is preserved as we did in thermal analysis and (iii) The stress field is calculated under plane strain assumption.

In Section 4-2, mechanical boundary conditions are applied on all the surfaces. The base plate bottom surface is clamped and the rest of the boundary conditions are traction free conditions. Temperature dependent material properties are introduced in Section 4-3, including Young's modulus, Poisson's ratio and thermal expansion coefficient. In Section 4-4, it is explained that the stress field is calculated only once for each layer after the cooling stage is finished and it is assumed the stress fields are time independent. The simulations are carried

out with different work piece geometry.

The simulation results are displayed in Section 4-5. From the results, it can be discovered that high residual stress is induced by either sharp temperature gradient on the top layers or the bottom boundary constraint. Besides, an obvious stress concentration occurs at the interface between the base plate and the work piece due to the sudden cross sectional area change in that region. Accordingly, it is suggested to reduce the residual stress by narrowing down the temperature gap between the top layers and protective gas in the cooling stage or avoiding positive inclination in work piece.

In Section 4-6, the comparison between the moving grid method and the element activation method shows that the moving grid method has a better performance in computational efficiency and also gives an accurate stress prediction.

Chapter 5

Conclusions and recommendations

In the previous chapters a novel moving grid method is introduced to solve the temperature field and stress field in the SLM process. The simulations are carried out under different process conditions defined by dimensionless parameters. The predictions of the moving grid simulations are compared with the results obtained by another popular SLM process modelling approach, which is the element activation method. In this chapter, several conclusions can be drawn with regard to the simulation results and some outlooks can be given for future work.

5-1 Conclusions

The purpose of our research is to develop a computationally efficient thermal-mechanical modelling approach that can shed light on what effects the process parameters will have on the temperature distribution and the stress field in the work piece.

A moving grid method is hence proposed, in which the growing domain of the SLM process is defined and described by the convective term in the governing equation. Both the heating stage and the cooling stage are taken into account in the model together with the corresponding thermal boundary conditions. Furthermore, the moving grid method is implemented by an explicit finite difference scheme based on a square mesh and subsequently the stability requirements are prescribed to calculate the allowable time step and spatial interval.

The process conditions and parameters are represented by 4 dimensionless parameters and these parameters are, dimensionless growth rate $\dot{H}$, Biot number Bi, heating/cooling ratio λ and work piece inclination γ. Thermal simulations are carried out with different combinations of these dimensionless parameters and several conclusions can be drawn from the simulation results.

Work piece with positive inclination tends to result in high average temperature while the average temperature level is low in those with negative inclination. The dimensionless growth rate has an impact on both the heating-cooling cycle duration and the average temperature. A higher dimensionless growth rate leads to shorter heating-cooling cycle duration as well as smaller temperature difference in a heating-cooling cycle. Increasing Biot number is capable

of reducing the average temperature in work piece but this effect is negligible. Smaller heating/cooling time ratio indicates a longer duration of cooling, which also lowers the average temperature level in the work piece.

Besides, the moving grid method shows a remarkable improvement in computational efficiency by comparing with the time cost of element activation method. The relative error of temperature predictions are within the acceptable range.

The thermal-mechanical coupling model is defined on the same domain as in thermal model with mechanical boundary conditions applied. Three assumptions are made in the stress analysis part:

- The work piece is purely elastic and it is assumed that the maximum stress will not exceed the yield strength.
- The cooling stage is simplified by resetting all the nodal temperature back to the room temperature in one time step and the heating stage is preserved as we did in thermal analysis.
- The stress field is calculated under the plane strain assumption.

Moreover, the temperature-dependent material properties are introduced to the model. The thermal-mechanical analysis is implemented on work piece with different inclinations. The simulation results prove that the sharp thermal gradient in top layers and the boundary constraint at the bottom will lead to a high level of stress. Additionally, in work piece with a positive inclination, a stress concentration can be observed at the interface of the work piece and the base plate due to the sudden change of cross sectional area. Therefore, measures can be taken to reduce the stress level from the aspects mentioned above. For example, try to decrease the temperature gap at the top surface or avoid building the part geometry with a positive inclination. The comparison between the moving grid method and the element activation method in the end not only shows the superiority of the moving grid method in computational efficiency, but also verifies the accuracy of moving grid method is sufficient.

As the final conclusion, the moving grid method introduced in this thesis greatly improves the computational efficiency in SLM process modelling and also provides credible predictions on the temperature field and the stress field. The relation between various process parameters and final part quality can be thus revealed by implementing this method.

5-2 Recommendations

For the outlook of future work, some recommendations can be given in the following aspects:

- The influence of dimensionless growth rate, heating/cooling time ratio and Biot number on stress field deserve further research as they are not mentioned in this thesis.
- It is possible to apply a nonlinear growth rate in thermal modelling rather than a linear one. By applying the nonlinear relation, the total number of elements in the moving grid is still identical in each time step but the height of the element is unevenly divided. For example, if $\partial y/\partial t$ is defined as $\dot{l}\sqrt{\zeta}$ rather than $\dot{l}\zeta$, then the grid on the top part of

the work piece is finer but grid at the bottom is coarser. Given that during the SLM process most of the physical changes happen on the top layers, the simulation accuracy for the top part can be further improved.

- Due to the finite resolution of the mesh elements, some numerical error may occur near the lateral boundaries during simulations. For instance, some artificial stress concentrations can be observed in part geometry with inclination. Thus it is advisable to consider an unstructured grid in the analysis.
- The explicit finite difference scheme may become a bottleneck for moving grid method because of the strict stability condition. Other options like implicit finite difference method or FEM can be taken into account to solve the thermal field.
- It is suggested to build the thermal-mechanical model by elastoplastic constitutive law for better prediction of stress results because the extreme residual stresses are very likely to exceed the material yield strength during the simulation process.

All in all, this novel moving grid method shows promising potential in computationally efficient thermal mechanical modelling. But there are still challenges and limitations within this method. It is expected that this thesis can provide some guidance for future research.

Appendix I

The idea of Von Neumann stability analysis

Assume we are concerned with the stability of a linear two time-level difference equation in $u(x,t)$ in the time interval $0 \leq t \leq T = Jk$, T finite, as $\delta x = h \to 0$ and $\delta t = k \to 0$, i.e. as $J \to \infty$. The Fourier series or von Neumann method expresses the initial values at the mesh points along $t = 0$ in terms of a finite Fourier series, then considers the growth of a function that reduces to this series for $t = 0$ by a 'variables separable' method identical to that commonly used for solving partial differential equations.

The Fourier series can be formulated in terms of sines and cosines but the algebra is easier if the complex exponential form is used, i.e. with $\sum a_n \cos(n\pi x/l)$ or $\sum b_n \sin(n\pi x/l)$ replaced by the equivalent $\sum A_n e^{in\pi x/l}$, where $i = \sqrt{-1}$ and l is the x-interval throughout which the function is defined. Clearly we need to change our usual notation $u_{i,j}$ to $u(ph, qk) = u_{p,q}$. In terms of this notation,

$$A_n e^{in\pi x/l} = A_n e^{in\pi ph/Nh} = A_n e^{i\beta_n ph}$$

where $\beta_n = n\pi/Nh$ and $Nh = l$.

Denote the initial values at the pivotal points along $t = 0$ by $u(ph, 0) = u_{p,0}$, $p = 0(1)N$. Then the N+1 equations

$$u_{p,0} = \sum_{n=0}^{N} A_n e^{i\beta_n ph}, p = 0, 1, ..., N$$

are sufficient to determine the $(N + 1)$ unknowns A_0,A_1,...,A_N uniquely, showing that the initial mesh values can be expressed in this complex exponential form. As we are considering only linear-difference equations we need investigate the propagation of only one initial value, such as $e^{i\beta ph}$, because separate solutions are additive, The coefficient A_n is a constant and can be neglected.

To investigate the propagation of this term as t increases, put

$$u_{p,q} = e^{i\beta x} e^{\alpha t} = e^{i\beta ph} e^{\alpha qk} = e^{i\beta ph} \xi^q$$

where $\xi = e^{\alpha k}$ and α, in general, is a complex constant. ξ is often called the amplification factor.

In most cases, the amplification factor needs to be satisfy the condition that $|\xi| \leq 1$ [29].

Calculation of stability

The governing equation of the one dimensional problem is

$$\frac{\partial \theta}{\partial \tau} = \frac{\partial^2 \theta}{\partial \zeta^2}\frac{1}{H^2} + \frac{\partial \theta}{\partial \zeta}\frac{\partial H}{\partial \tau}\frac{\zeta}{H} \tag{1}$$

then the finite difference computational scheme is

$$\frac{u_{p,q+1} - u_{p,q}}{\Delta \tau} = \frac{\zeta}{H}\dot{H}\frac{u_{p+1,q} - u_{p-1,q}}{2\Delta\zeta} + \frac{1}{H^2}\frac{u_{p+1,q} - 2u_{p,q} + u_{p-1,q}}{\Delta\zeta^2} \tag{2}$$

further simplification can be made in the equation above,

$$u_{p,q+1} - u_{p,q} = \frac{ph}{H}\dot{H}\frac{\Delta\tau}{2h}\left(u_{p+1,q} - u_{p-1,q}\right) + \frac{1}{H^2}\frac{\Delta\tau}{h^2}\left(u_{p+1,q} - 2u_{p,q} + u_{p-1,q}\right) \tag{3}$$

$$= r\frac{ph^2\dot{H}}{2H}\left(u_{p+1,q} - u_{p-1,q}\right) + \frac{r}{H^2}\left(u_{p+1,q} - 2u_{p,q} + u_{p-1,q}\right) \tag{4}$$

in which $r = \frac{\Delta\tau}{\Delta\zeta^2}$ and $h = \Delta X$ or $\Delta\zeta$.

Substitution of $u_{p,q} = e^{i\beta ph}\xi^q$ into the difference equation shows that

$$e^{i\beta ph}\xi^{q+1} - e^{i\beta ph}\xi^q = r\frac{ph^2\dot{H}}{2H}\left(e^{i\beta(p+1)h}\xi^q - e^{i\beta(p-1)h}\xi^q\right) + \frac{r}{H^2}\left(e^{i\beta(p+1)h}\xi^q - 2e^{i\beta ph}\xi^q + e^{i\beta(p-1)h}\xi^q\right) \tag{5}$$

Division by $e^{i\beta ph}\xi^q$ leads to

$$\xi - 1 = r\frac{ph^2\dot{H}}{2H}\left(e^{i\beta h} - e^{-i\beta h}\right) + \frac{r}{H^2}\left(e^{i\beta h} - 2 + e^{-i\beta h}\right) \tag{6}$$

$$= r\frac{ph^2\dot{H}}{2H}2i\sin\alpha - \frac{r}{H^2}4\sin^2\frac{\alpha}{2} \tag{7}$$

thus

$$\xi = 1 - 4\frac{r}{H^2}\sin^2\frac{\alpha}{2} + r\frac{ph^2\dot{H}}{H}i\sin\alpha \tag{8}$$

In order to check the stability condition,

$$|\xi|^2 = 1 + 16\frac{r^2}{H^4}\sin^4\frac{\alpha}{2} - 8\frac{r}{H^2}\sin^2\frac{\alpha}{2} + r^2\frac{p^2h^4\dot{H}^2}{H^2}\sin^2\alpha \tag{9}$$

$$= 1 + 16\frac{r^2}{H^4}\sin^4\frac{\alpha}{2} - 4r\sin^2\frac{\alpha}{2}\left(\frac{2}{H^2} - r\frac{p^2h^4\dot{H}^2}{H^2}\cos^2\frac{\alpha}{2}\right) \tag{10}$$

the stability condition indicates

$$|\xi|^2 = 1 + 16\frac{r^2}{H^4}\sin^4\frac{\alpha}{2} - 4r\sin^2\frac{\alpha}{2}\left(\frac{2}{H^2} - r\frac{p^2h^4\dot{H}^2}{H^2}\cos^2\frac{\alpha}{2}\right) \leq 1 \tag{11}$$

which means

$$16\frac{r^2}{H^4}\sin^4\frac{\alpha}{2} - 4r\sin^2\frac{\alpha}{2}\left(\frac{2}{H^2} - r\frac{p^2h^4\dot{H}^2}{H^2}\cos^2\frac{\alpha}{2}\right) \leq 0 \tag{12}$$

then

$$4r\sin^2\frac{\alpha}{2}\left(\frac{2}{H^2} - r\frac{p^2h^4\dot{H}^2}{H^2}\cos^2\frac{\alpha}{2}\right) \geq 16\frac{r^2}{H^4}\sin^4\frac{\alpha}{2}\frac{2}{H^2} - r\frac{p^2h^4\dot{H}^2}{H^2}\cos^2\frac{\alpha}{2} \tag{13}$$

$$\geq 16\frac{r^2}{H^4}\sin^4\frac{\alpha}{2}2 - rp^2h^4\dot{H}^2\cos^2\frac{\alpha}{2} \tag{14}$$

$$\geq \frac{4r}{H^2}\sin^2\frac{\alpha}{2} \tag{15}$$

Therefore,

$$r = \frac{\Delta\tau}{h^2} \leq \frac{2}{\frac{4}{H^2}\sin^2\frac{\alpha}{2} + p^2h^4\dot{H}^2\cos^2\frac{\alpha}{2}} > \frac{2}{\frac{4}{H^2} + p^2h^4\dot{H}^2} \tag{16}$$

so we have

$$\frac{\Delta\tau}{h^2} < \frac{2}{\frac{4}{H^2} + p^2h^4\dot{H}^2} \tag{17}$$

what's more, $p^2h^2 = \zeta_p^2 \leq 1$, therefore,

$$\Delta\tau < \frac{2h^2}{\frac{4}{H^2} + \left(h\dot{H}\right)^2} \tag{18}$$

the range of H is between 1 and 4, the larger H is, the larger RHS is, then

$$\Delta\tau < \frac{2h^2}{4 + \left(h\dot{H}\right)^2} \tag{19}$$

Appendix II

Cluster settings

The PME cluster consists of

- 10 nodes equipped with 48 AMD Opteron CPUs (6344, 2.6 GHz, 4 x 12 cores) and 192 GB RAM each. (Nodes 95-98, 143-148)
- 1 node equipped with a 10-core Intel Xeon CPU (E5-2680v2, 2.8 GHz), 128 GB RAM and 2 nVidia Tesla X20 GPU cards (Node 149)
- 4 nodes equipped with 6-core Intel Xeon CPUs (E5-2643v3, 3.4 GHz) and 128 GB RAM each (Nodes 01 – 16)
- 12 nodes equipped with 8-core Intel Xeon CPUs (E5-2630v3, 2.4 GHz) and 128 GB RAM each (Nodes 01 – 16)

Node 149 only uses for large-scale parallel computing which is not accessible with my authority. The other nodes are the tools for running my simulation, when a job is submitted, the terminal will assign a vacant node randomly to run your simulation. Although there is slight variation with their computational ability, that will not make a remarkable difference in computational time.

Bibliography

[1] W. E. Frazier, "Metal additive manufacturing: A review," *Journal of Materials Engineering and Performance*, vol. 23, pp. 1917–1928, Jun 2014.

[2] C.Körner, E. Attar, and P. Heinl, "Mesoscopic simulation of selective beam melting processes," *Journal of Materials Processing Technology*, vol. 211, no. 6, pp. 978 – 987, 2011.

[3] M. M. Francois, A. Sun, W. E. King, H. Jon, T.Damien, B. C. Allan, N. N. Carlson, C. K. Newman, T. S. Haut, J. Bakosi, J. W. Gibbs, V. Livescu, S. A. Vander Wiel, A. J. Clarke, M. W. Schraad, T. Blacker, H. Lim, T. Rodgers, S. Owen, F. Abdeljawad, J. Madison, A. T. Anderson, J. L. Fattebert, R. M. Ferencz, N. E. Hodge, S. A. Khairallah, and O. Walton, "Modeling of additive manufacturing processes for metals: Challenges and opportunities," *Current Opinion in Solid State and Materials Science*, vol. 21, 1 2017.

[4] L.Nicholas, S. Brown, J. Sienz, C.John, and B. Fawzi, "A review of computational modelling of additive layer, manufacturing - multi-scale and multi-physics," 04 2014.

[5] N. E. Hodge, R. M. Ferencz, and J. M. Solberg, "Implementation of a thermomechanical model for the simulation of selective laser melting," *Computational Mechanics*, vol. 54, pp. 33–51, Jul 2014.

[6] B.Cheng, S.Shrestha, and K.Chou, "Stress and deformation evaluations of scanning strategy effect in selective laser melting," *Additive Manufacturing*, vol. 12, pp. 240 – 251, 2016. Special Issue on Modeling Simulation for Additive Manufacturing.

[7] K. V. Wong and A. Hernandez, "A review of additive manufacturing," *ISRN Mechanical Engineering*, vol. 2012, p. 10, 2012.

[8] M.Matthias and K. Carolin, "Multiscale modeling of powder bed–based additive manufacturing," *Annual Review of Materials Research*, vol. 46, no. 1, pp. 93–123, 2016.

[9] I. Campbell, O. Diegel, J. Kowen, and T. Wohlers, *Wohlers Report 2017 3D Printing and Additive Manufacturing State of the Industry: Annual Worldwide Progress Report*. Wohlers Associates, 2017.

[10] C. H. Fu and Y. B. Guo, "Three-Dimensional Temperature Gradient Mechanism in Selective Laser Melting of Ti-6Al-4V," *Journal of Manufacturing Science and Engineering*, vol. 136, 10 2014. 061004.

[11] Z. Luo and Y. Zhao, "A survey of finite element analysis of temperature and thermal stress fields in powder bed fusion additive manufacturing," *Additive Manufacturing*, vol. 21, pp. 318 – 332, 2018.

[12] A. Gusarov, I. Yadroitsev, P. Bertrand, and I. Smurov, "Heat transfer modelling and stability analysis of selective laser melting," *Applied Surface Science*, vol. 254, no. 4, pp. 975 – 979, 2007. Laser synthesis and processing of advanced materials.

[13] P. Collins, D. Brice, P. Samimi, I. Ghamarian, and H. Fraser, "Microstructural control of additively manufactured metallic materials," *Annual Review of Materials Research*, vol. 46, no. 1, pp. 63–91, 2016.

[14] M.Mustafa, M.Hans-Wilfried, N. N'Dri, D. Hongzhi, and D.Olivier, "Metal additive-manufacturing process and residual stress modeling," *Integrating Materials and Manufacturing Innovation*, vol. 5, pp. 61–93, Dec 2016.

[15] M.Chiumenti, E.Neiva, E.Salsi, M.Cervera, S.Badia, J.Moya, Z.Chen, C.Lee, and C.Davies, "Numerical modelling and experimental validation in selective laser melting," *Additive Manufacturing*, vol. 18, pp. 171 – 185, 2017.

[16] K. Zeng, D. Pal, and S.Brent, "A review of thermal analysis methods in laser sintering and selective laser melting," *23rd Annual International Solid Freeform Fabrication Symposium - An Additive Manufacturing Conference, SFF 2012*, pp. 796–814, 01 2012.

[17] B.Schoinochoritis, D.Chantzis, and K.Salonitis, "Simulation of metallic powder bed additive manufacturing processes with the finite element method: A critical review," *Proceedings of the Institution of Mechanical Engineers, Part B: Journal of Engineering Manufacture*, vol. 231, no. 1, pp. 96–117, 2017.

[18] T. H. C. Childs, M. Berzins, G. R. Ryder, and A. Tontowi, "Selective laser sintering of an amorphous polymer—simulations and experiments," *Proceedings of the Institution of Mechanical Engineers, Part B: Journal of Engineering Manufacture*, vol. 213, no. 4, pp. 333–349, 1999.

[19] P.Nachiket, P.Deepankar, H. Khalid Rafi, Z.Kai, M.Alleyce, H.Adam, B.David, and S.Brent, "A Generalized Feed Forward Dynamic Adaptive Mesh Refinement and Derefinement Finite Element Framework for Metal Laser Sintering—Part I: Formulation and Algorithm Development," *Journal of Manufacturing Science and Engineering*, vol. 137, 08 2015. 041001.

[20] Y. Yang, M. Knol, F. van Keulen, and C. Ayas, "A semi-analytical thermal modelling approach for selective laser melting," *Additive Manufacturing*, vol. 21, pp. 284 – 297, 2018.

[21] M.Peters, "Residual stresses in selective laser sintering and selective laser melting," *Rapid Prototyping Journal*, vol. 12, pp. 254–265, 2006.

[22] D.Munro, C.Ayas, M.Langelaar, and F. Keulen, "On process-step parallel computability and linear superposition of mechanical responses in additive manufacturing process simulation," *Additive Manufacturing*, vol. 28, pp. 738 – 749, 2019.

[23] P. Guduru, E. Chason, and L. Freund, "Mechanics of compressive stress evolution during thin film growth," *Journal of the Mechanics and Physics of Solids*, vol. 51, no. 11, pp. 2127 – 2148, 2003. Proceedings of a Symposium on Dynamic Failure and Thin Film Mechanics, honoring Professor L.B. Freund.

[24] R. M. FURZELAND, "A Comparative Study of Numerical Methods for Moving Boundary Problems," *IMA Journal of Applied Mathematics*, vol. 26, pp. 411–429, 12 1980.

[25] G. Marshall, "A front tracking method for one-dimensional moving boundary problems," *SIAM Journal on Scientific and Statistical Computing*, vol. 7, no. 1, pp. 252–263, 1986.

[26] J. Crank, *Free and moving boundary problems*. Oxford University Press, 1987.

[27] R. S. Gupta, "Moving grid method without interpolations," *Computer Methods in Applied Mechanics and Engineering*, vol. 4, no. 2, pp. 143–152, 1974.

[28] S. Kutluay, A. Bahadir, and A. Özdeş, "The numerical solution of one-phase classical stefan problem," *Journal of computational and applied mathematics*, vol. 81, no. 1, pp. 135–144, 1997.

[29] G. D. Smith, G. D. Smith, and G. D. S. Smith, *Numerical solution of partial differential equations: finite difference methods*. Oxford university press, 1985.

[30] C. S. Kim, "Thermophysical properties of stainless steels," tech. rep., Argonne National Lab., Ill.(USA), 1975.

[31] G. Additive, "M2 series 5," 2019. "https://www.ge.com/additive/additive-manufacturing/machines/m2series5", Sidst set 06/10/2020.

[32] L. Murr, "Metallurgy of additive manufacturing: Examples from electron beam melting," *Additive Manufacturing*, vol. 5, pp. 40–53, 2015.

[33] G. Pottlacher, H. Hosaeus, E. Kaschnitz, and A. Seifter, "Thermophysical properties of solid and liquidinconel 718 alloy," *Scandinavian Journal of Metallurgy*, vol. 31, no. 3, pp. 161–168, 2002.

[34] M. Boivineau, C. Cagran, D. Doytier, V. Eyraud, M.-H. Nadal, B. Wilthan, and G. Pottlacher, "Thermophysical properties of solid and liquid ti-6al-4v (ta6v) alloy," *International journal of thermophysics*, vol. 27, no. 2, pp. 507–529, 2006.

[35] A. F. Mills, *Basic heat and mass transfer*. Prentice hall, 1999.

[36] J. Ding, P. Colegrove, J. Mehnen, S. Ganguly, P. S. Almeida, F. Wang, and S. Williams, "Thermo-mechanical analysis of wire and arc additive layer manufacturing process on large multi-layer parts," *Computational Materials Science*, vol. 50, no. 12, pp. 3315–3322, 2011.

[37] J. L. Bartlett and X. Li, "An overview of residual stresses in metal powder bed fusion," *Additive Manufacturing*, vol. 27, pp. 131–149, 2019.

[38] COMSOL, "Material library," 2020. "https://www.comsol.nl/material-library", Sidst set 10/10/2020.

[39] E. R. Denlinger, M. Gouge, J. Irwin, and P. Michaleris, "Thermomechanical model development and in situ experimental validation of the laser powder-bed fusion process," *Additive Manufacturing*, vol. 16, pp. 73–80, 2017.

[40] R. J. Williams, C. M. Davies, and P. A. Hooper, "A pragmatic part scale model for residual stress and distortion prediction in powder bed fusion," *Additive Manufacturing*, vol. 22, pp. 416–425, 2018.